Astronomy & Astrophysics manuscript no. aa
December 10, 2015
©ESO 2015

arXiv:1512.02986v1 [astro-ph.SR] 9 Dec 2015

Deuterium Fractionation in the Ophiuchus Molecular Cloud⋆

A. Punanova[1], P. Caselli[1], A. Pon[2], A. Belloche[3] and Ph. André[4]

[1] Max-Planck-Institut für extraterrestrische Physik, Giessenbachstrasse 1, 85748 Garching, Germany
e-mail: punanova@mpe.mpg.de
[2] Department of Physics and Astronomy, The University of Western Ontario, London, ON, N6A 3K7, Canada
[3] Max-Planck-Institut für Radioastronomie, Auf dem Hügel 69, D-53121 Bonn, Germany
[4] IRFU/SAp CEA/DSM, Laboratoire AIM CNRS — Université Paris Diderot, 91191 Gif-sur-Yvette, France

Received October 19, 2015; accepted December 09, 2015

ABSTRACT

Context. In cold ($T < 25$ K) and dense ($n_H > 10^4$ cm^{-3}) interstellar clouds, molecules like CO are significantly frozen onto dust grain surfaces. Deuterium fractionation is known to be very efficient in these conditions as CO limits the abundance of H_3^+, the starting point of deuterium chemistry. In particular, N_2D^+ is an excellent tracer of dense and cold gas in star forming regions.
Aims. We measure the deuterium fraction, R_D, and the CO-depletion factor, f_d, toward a number of starless and protostellar cores in the L1688 region of the Ophiuchus molecular cloud complex and search for variations based upon environmental differences across L1688. The kinematic properties of the dense gas traced by the N_2H^+ and N_2D^+ (1–0) lines are also discussed.
Methods. R_D has been measured via observations of the J = 1–0 transition of N_2H^+ and N_2D^+ toward 33 dense cores in different regions of L1688. f_d estimates have been done using $C^{17}O$(1–0) and 850 μm dust continuum emission from the SCUBA survey. All line observations were carried out with the IRAM 30 meter antenna.
Results. The dense cores show large (≃2–40%) deuterium fractions, with significant variations between the sub-regions of L1688. The CO-depletion factor also varies from one region to another (between ≃1 and 7). Two different correlations are found between deuterium fraction and CO-depletion factor: cores in regions A, B2 and I show increasing R_D with increasing f_d, similar to previous studies of deuterium fraction in pre-stellar cores; cores in regions B1, B1B2, C, E, F and H show a steeper R_D–f_d correlation, with large deuterium fractions occurring in fairly quiescent gas with relatively low CO freeze-out factors. These are probably recently formed, centrally concentrated starless cores which have not yet started the contraction phase toward protostellar formation. We also find that the deuterium fraction is affected by the amount of turbulence, dust temperature and distance from heating sources in all regions of L1688, although no clear trend is found.
Conclusions. The deuterium fraction and amount of CO freeze-out are sensitive to environmental conditions and their variations across L1688 show that regions of the same molecular cloud experience different dynamical, thermal and chemical histories, with consequences for the current star formation efficiency and the characteristics of future stellar systems. The large pressures present in L1688 may induce the formation of small dense starless cores, unresolved with our beam, where the R_D–f_d relation appears to deviate from that expected from chemical models. We predict that high angular resolution observations will reconcile observations with theory.

Key words. Stars:formation – ISM: kinematics and dynamics – ISM: clouds – ISM: abundances – ISM: molecules

1. Introduction

The first stages of the star formation process are dense starless and self-gravitating cores, i.e. the so-called pre-stellar cores (Ward-Thompson et al. 1999; Crapsi et al. 2005). Pre-stellar cores in nearby star forming regions are typically cold (∼10 K), dense (10^4–10^7 cm^{-3}) and quiescent (thermal pressure dominates over turbulent motions; e.g. Benson & Myers 1989; Fuller & Myers 1992; Lada et al. 2008; Keto & Caselli 2008).

Chemical differentiation takes place in pre-stellar cores (see e.g. Bergin & Tafalla 2007; di Francesco et al. 2007; Caselli 2011, for reviews). While CO is the second most abundant molecule in the interstellar medium, it tends to freeze onto dust grains in the dense, cold conditions at the centres of pre-stellar cores (e.g. Caselli et al. 1999; Bacmann et al. 2002). The level of CO depletion is usually measured as $f_d = X_{ref}(\mathrm{CO})/N(\mathrm{CO}) \cdot N(\mathrm{H_2})$, where X_{ref}(CO) is the reference value of the CO fractional abundance, typically between 1 and 2×10^{-4} (e.g. Frerking et al. 1982; Lacy et al. 1994). The typical value of the CO-depletion factor in pre-stellar cores is 5–20 (Crapsi et al. 2005; Christie et al. 2012).

In such cold and dense gas, deuterated species are preferentially formed (e.g. Caselli & Ceccarelli 2012). H_2D^+ is responsible for the enhancement of the deuterium fraction in most molecular species and is formed by the deuteron-proton exchange reaction $H_3^+ + HD \rightleftharpoons H_2D^+ + H_2 + 230$ K (Millar et al. 1989). The deuteron-proton exchange reaction is exothermic and does not proceed from right to left at temperatures lower than 30 K and if most of the H_2 molecules are in para form (e.g. Pagani et al. 1992). H_2D^+ then reacts with other species to form deuterated ions via $H_2D^+ + A \rightarrow AD^+ + H_2$, where A can be any of CO, N_2 and other neutral species (Herbst & Klemperer 1973; Dalgarno & Lepp 1984). When CO and other abundant neutral species, which destroy H_3^+ and H_2D^+, are severely frozen onto dust grain surfaces, the deuterium fraction becomes significant. For example, the deuterium fraction in pre-stellar cores is 5–50%, while the elemental abundance of deuterium is ∼1.5×10^{-5} with respect

⋆ Based on observations carried out with the IRAM 30m Telescope. IRAM is supported by INSU/CNRS (France), MPG (Germany) and IGN (Spain).

to hydrogen atoms within 1 kpc of the Sun (Linsky et al. 2006; Caselli 2011).

In particular, the deuterium fraction of N_2H^+ has been used to identify the earliest phases of star-formation, as the N_2H^+ deuterium fraction peaks at the pre-stellar phase and toward the youngest protostars (Crapsi et al. 2005; Emprechtinger et al. 2009; Friesen et al. 2013; Fontani et al. 2014). The deuterium fraction in N_2H^+ is usually given as $R_D = N(N_2D^+)/N(N_2H^+)$, where $N(i)$ is the column density of species i.

L1688 is a nearby, 120 pc distant (Lombardi et al. 2008) low-mass star forming region within the Ophiuchus Molecular Cloud Complex. The multiple star forming regions within L1688 contain more than 60 dense cores and 50 young stellar objects in different evolutionary stages (Motte et al. 1998; André et al. 2007; Simpson et al. 2008; Pattle et al. 2015). L1688 is divided into 10 regions (A–I; see Fig. 1) with different environmental properties. For instance, while the gas temperature is relatively constant within each region, it varies significantly from one region to another (≃10–17 K; Friesen et al. 2009).

The deuterium fraction across the entirety of L1688 has not been systematically studied yet. For only a few regions has the deuterium fraction been measured, for example the B2 region has an average R_D ∼3% (Friesen et al. 2010). CO-depletion across the whole of Ophiuchus has been found to be relatively low compared to the other Gould Belt star-forming regions, with an average value less than 10 (Gurney et al. 2008; Christie et al. 2012).

In this paper, we present observations of N_2D^+(1–0), N_2D^+(2–1), N_2H^+(1–0), $C^{17}O$(1–0) and $C^{17}O$(2–1) towards 40 cores to measure the deuterium fraction and CO depletion factor across the entire L1688 region. In Section 2, details regarding the observations are presented. Section 3 describes the results of hyperfine structure fitting as well as deuterium fraction and CO-depletion calculations. In Section 4, we discuss the results and their relation to possible environmental effects. The conclusions are given in Section 5.

2. Observations and data reduction

Figure 1 shows the L1688 region mapped in 850 μm dust continuum emission (Di Francesco et al. 2008). 40 dense cores, revealed by Motte et al. (1998) with 1.3 mm dust emission mapping, were selected for observation with the IRAM 30 meter telescope and are shown with filled blue squares. The names and positions of the cores are given in Table A.1. Figure 1 also shows the positions of young stellar objects (YSOs) embedded in the cloud as open circles (Motte et al. 1998; Simpson et al. 2008; Dunham et al. 2015). The molecular line observations were performed with the IRAM 30 meter telescope in June 1998, July 2000 and December 2004. The following transitions were observed: N_2D^+(1–0), N_2D^+(2–1), N_2D^+(3–2), N_2H^+(1–0), N_2H^+(3–2), $C^{17}O$(1–0) and $C^{17}O$(2–1). The observations were obtained with the AB receiver and the VESPA backend. Typical system temperatures for the (1–0) transition observations were 100–200 K for N_2H^+–N_2D^+ and 200–360 K for the $C^{17}O$ line. The spectral resolution for the N_2H^+, N_2D^+ and $C^{17}O$ (1–0) lines varied from 6.5 to 40 kHz and the angular resolutions were 22, 32.1 and 26.6 arc seconds for $C^{17}O$(1–0), N_2D^+(1–0) and N_2H^+(1–0), respectively (see Table 1). The spectra were taken using the position switching (datasets 051-00 and 188-97) and frequency switching (dataset 066-04, with a frequency throw of 7.8 MHz) modes. In Table 1, the dates of the observing runs are given and each run denoted with a dataset number.

The data reduction was performed with the CLASS package[1]. For each source, there were several spectra of the same line. These spectra have been adjusted to have the same central frequency and summed together to improve the sensitivity. The integration time for different lines and objects varies from 4 to 30 minutes. The intensity scale was converted to the main-beam temperature scale according to the beam efficiency values given in Table 1.

The N_2D^+(1–0), N_2D^+(2–1), N_2H^+(1–0), $C^{17}O$(1–0) and $C^{17}O$(2–1) lines have hyperfine splitting with 15, 40, 15, 3 and 9 components respectively. As such, the spectra were analysed using the standard CLASS hyperfine structure (hfs) fitting method. The routine computes line profiles, with the assumptions of Gaussian velocity distribution and equal excitation temperatures for all hyperfine components. The rest frequencies of the main components, the velocity offsets and the relative intensities of the hyperfine components of the lines were taken from Frerking & Langer (1981), Pagani et al. (2009) and Dore, L. (private communication). The N_2D^+(3–2) and N_2H^+(3–2) spectra have very poor baselines and reconstruction of the signal is not possible, so these data are not considered hereafter in the paper.

All spectra were initially fit assuming one velocity component. The hfs fitting routine returns both the rms of the baseline and the region with the spectral line. In case the rms of the spectral line region was greater than the rms of the baseline by a factor of 1.5, we redid the fit with an additional velocity component. This was repeated until the two rms agreed within a factor of 1.5. The largest number of velocity components needed was three.

3. Results

3.1. Spectra

The spectra of the N_2D^+(1–0), N_2H^+(1–0) and $C^{17}O$(1–0) lines are shown in Fig. 2. The N_2H^+(1–0), $C^{17}O$(1–0) and $C^{17}O$(2–1) emission was detected toward all 40 observed cores. N_2D^+(1–0) emission was detected toward 23 out of 33 observed cores and N_2D^+(2–1) emission was detected toward 25 out of 32 observed cores, with the A-MM4 core only having (2–1) detection. As the aim of the study is the measurement of deuterium fractions and their comparison to CO-depletion factors, we focus on the (1–0) transitions for the remainder of the paper, since they have the most similar beam sizes and excitation conditions. Toward five cores (B1-MM3, B1-MM4, B2-MM2, B2-MM8 and F-MM2), the N_2H^+(1–0) line shows two velocity components. The $C^{17}O$(1–0) line toward all of the objects in regions C (except C-Ne and C-MM3) and E and one in A (SM1N) shows two or three velocity components. The $N_2D^+(1-0)$ line shows two velocity components toward one core, B1-MM4. The results of the hfs fits are given in Tables A.2–A.6.

The centroid velocities, V_{LSR}, are determined from the hfs fitting and vary across L1688 from 3.3 to 4.6 km s^{-1} with a velocity generally increasing from region A to F. Figure 3 shows the centroid velocities for the N_2H^+(1–0), N_2D^+(1–0) and $C^{17}O$(1–0) lines. If two velocity components are detected in N_2H^+(1–0) and N_2D^+(1–0) (e.g. toward B1-MM4), both components are plotted in the left panel of Fig. 3. If only N_2H^+(1–0) shows two components we instead plot an average of the two components if the single N_2D^+(1–0) line component appears to be a blend of multiple component (cores B2-MM2, B2-MM8 and F-MM2),

[1] Continuum and Line Analysis Single-Dish Software http://www.iram.fr/IRAMFR/GILDAS

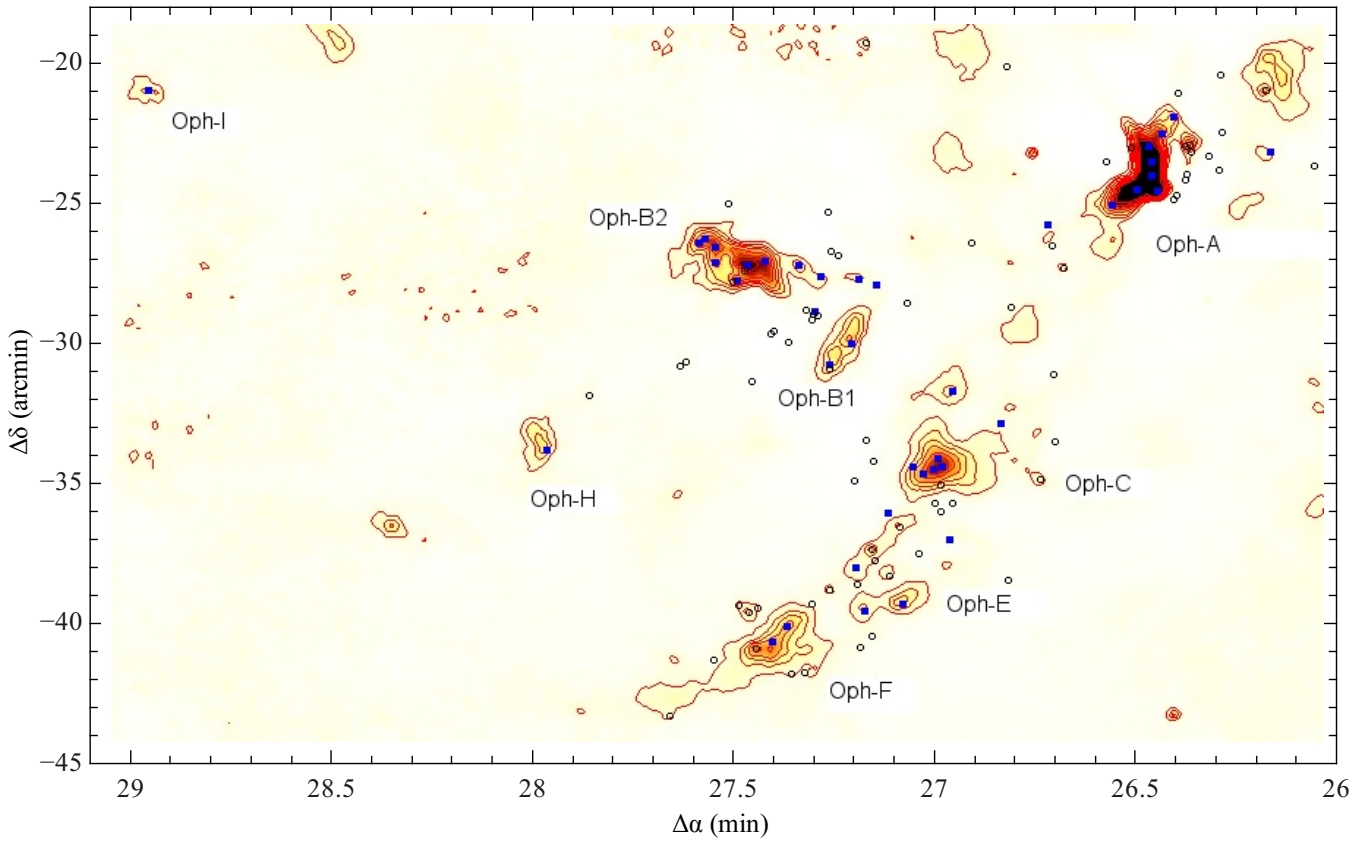

Fig. 1. 850 μm continuum emission of the L1688 region mapped by the Submillimeter Common-User Bolometer Array (SCUBA, Di Francesco et al. 2008), the beam size is 22.″9. Contour levels go from 0.2 Jy beam^{-1} in steps of 0.2 Jy beam^{-1} (3σ). The dense cores studied here are marked by filled blue squares and young stellar objects by open circles. The (0,0) offsets correspond to the J2000 equatorial position α = 16^{h}00^{m}00^{s}, δ = −24°00′00″. The fits file used to produce this map is available at http://www.cadc-ccda.hia-iha.nrc-cnrc.gc.ca/data/pub/JCMTSL/scuba_F_850umemi, file name scuba_F_353d1_16d8_850um.emi.fits.

and we plot just the velocity of the closest N_2H^+(1–0) component if the N_2D^+(1–0) component does not appear to be blended, with the second N_2D^+(1–0) component presumably not being detected above the noise level (core B1-MM3). The three cases are illustrated in Fig. 4. However, only a small fraction of the points (4/25) shown in Fig. 3 are for locations with different numbers of components detected in the two different tracers. For the right panel of Fig. 3, we plot each N_2H^+(1–0) component against the closest $C^{17}O$(1–0) component.

For 80% of the cores, the V_{LSR} of the N_2H^+(1–0) and N_2D^+(1–0) lines are within 0.05 km s^{-1} of each other. The largest centroid velocity difference is only 0.21 km s^{-1}. The $C^{17}O$(1–0) and N_2H^+(1–0) V_{LSR} can differ significantly with discrepancies up to 1 km s^{-1}. 51% of the cores have velocities that differ by over 0.1 km s^{-1}. This suggests that N_2H^+(1–0) and N_2D^+(1–0) trace roughly the same gas while $C^{17}O$(1–0) likely traces more extended gas, as expected considering the widespread distribution of CO in molecular clouds and its freeze-out in dense cold regions.

The line widths (full width at half maximum, FWHM, hereinafter Δv) of N_2H^+, N_2D^+ and $C^{17}O$ (1–0) are shown on Fig. 5. As before, when N_2H^+ and N_2D^+ show two velocity components, we plot them separately (B1-MM4). In the case where two velocity components are present in N_2H^+ and only one is seen in N_2D^+, we either take the Δv of N_2H^+ of the component with the closest V_{LSR}, if it appears that one component of

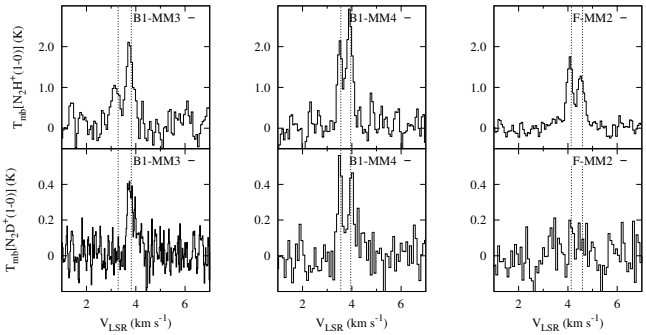

Fig. 4. Isolated hyperfine components of N_2H^+ and N_2D^+ (1–0) toward cores where two velocity components are found. The spectra are centred at the frequency of the isolated component. The dotted lines show the centroid velocities of the N_2H^+(1–0) components.

N_2D^+ is missing due to the noise level (B1-MM3), or we take $\Delta v = \Delta v_1/2 + \Delta v_2/2 + |V_{LSR1} - V_{LSR2}|$ if the N_2D^+ line appears to be a blend of two components (B2-MM2, B2-MM8, F-MM2). The three cases are shown in Fig. 4. For the comparison of the N_2H^+

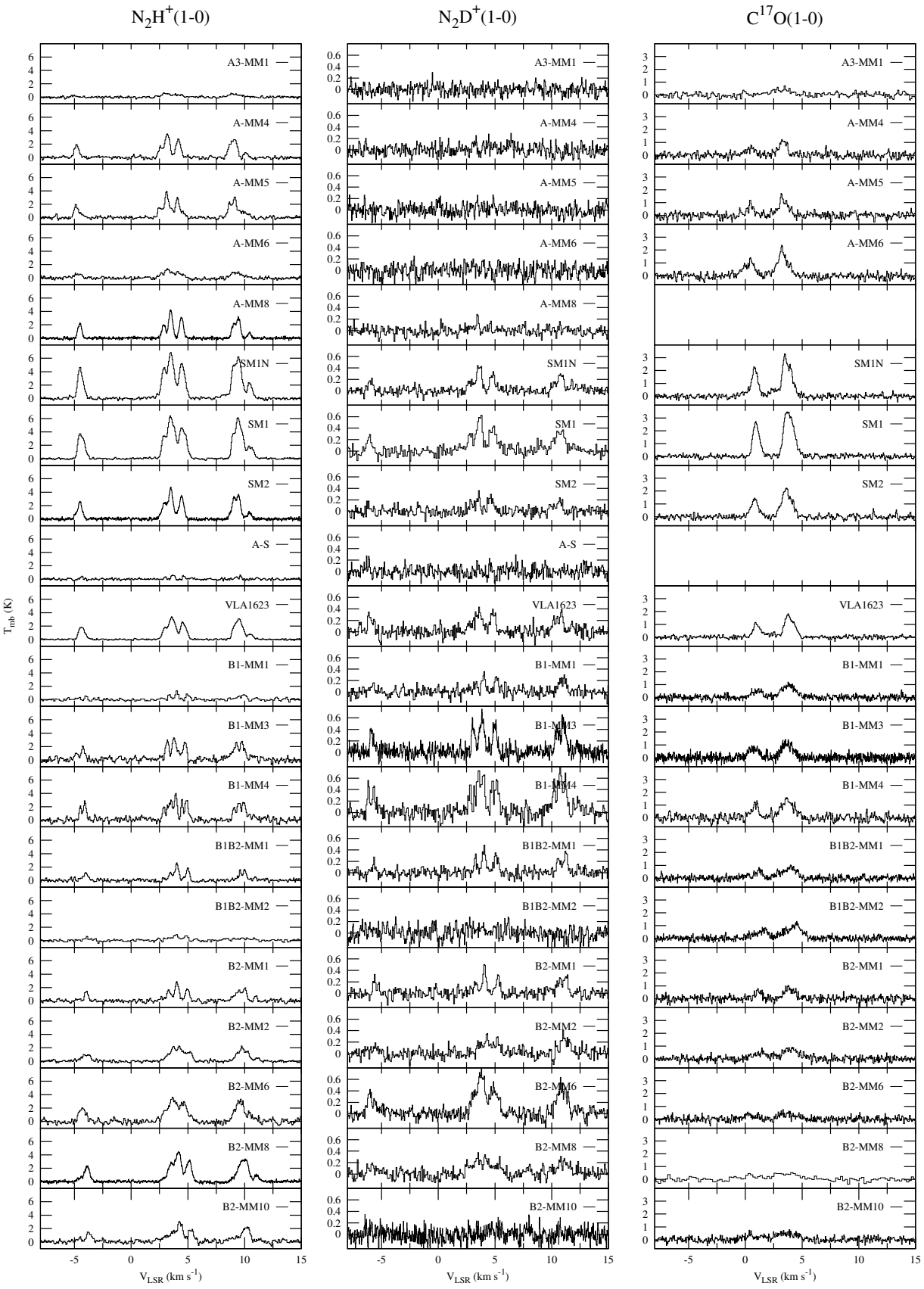

Fig. 2. N_2H^+(1-0), N_2D^+(1-0) and $C^{17}O$(1–0) spectra toward the observed dense cores, labeled in each panel.

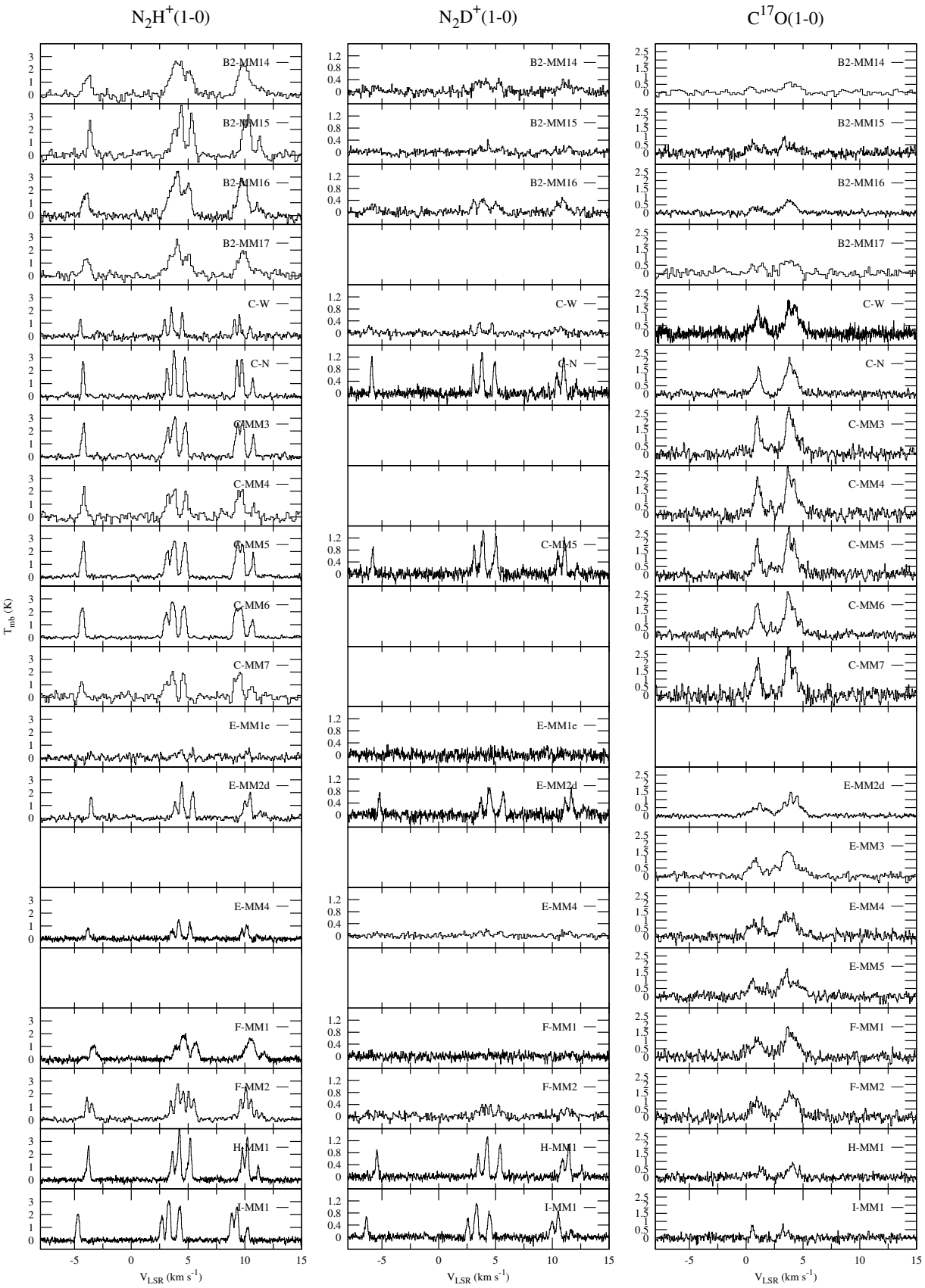

Fig. 2. N_2H^+(1-0), N_2D^+(1-0) and $C^{17}O$(1–0) spectra toward the observed dense cores, labeled in each panel (continuation).

Table 1. Observation parameters.

Species	Frequency[a] (GHz)	F_{eff}	B_{eff}[f]	HPBW (″)	Δv_{res}[g] (km s^{-1})	rms in T_{mb} (K)	T_{sys} (K)	Dates	Dataset[h]
N_2H^+(1–0)	93.1737637[b]	0.95	0.76	26.5	0.021	0.121	155–176	16.08.2004	066-04
N_2H^+(1–0)	93.1737637	0.92	0.78	26.5	0.063	0.089	114–205	11–16.07.2000	051-00
N_2H^+(1–0)	93.1737637	0.92	0.73	26.5	0.063	0.174	173–216	26–28.06.1998	188-97
N_2H^+(3–2)	279.511832[b]	0.87	0.46	8.8	0.021		652–2739	12–13.08.2004	066-04
N_2D^+(1–0)	77.1096162[b]	0.95	0.76	32.1	0.025	0.103	167–216	12–17.08.2004	066-04
N_2D^+(2–1)	154.2171805[c]	0.94	0.64	16.3	0.013	0.225	203–627	12–15.08.2004	066-04
N_2D^+(3–2)	231.3219119[c]	0.90	0.52	10.8	0.025		244–710	16.08.2004	066-04
$C^{17}O$(1–0)	112.358988[d]	0.95	0.78	22.0	0.017	0.218	243–320	16.08.2004	066-04
$C^{17}O$(1–0)	112.358988	0.92	0.78	22.0	0.052	0.143	184–289	12.07.2000	051-00
$C^{17}O$(1–0)	112.358988	0.92	0.73	22.0	0.052	0.180	265–359	29–30.06.1998	188-97
$C^{17}O$(2–1)	224.714370[e]	0.85	0.53	11.0	0.532	0.626	629–1366	13-16.07.2000	051-00
$C^{17}O$(2–1)	224.714370	0.90	0.42	11.0	0.052	0.977	995-1800	29–30.06.1998	188-97

[a] Frequency of the main hyperfine component; [b] from Pagani et al. (2009); [c] from Pagani et al. (2009) and Dore, L., private communication; [d] from Frerking & Langer (1981); [e] from SPLATALOGUE database http://www.cv.nrao.edu/php/splat/; [f] B_{eff} values are available at the 30 m antenna efficiencies web-page https://www.iram.fr/IRAMFR/ARN/aug05/node6.html; [g] Δv_{res} is the velocity resolution; [h] dataset name is the ID of the corresponding IRAM 30 m project.

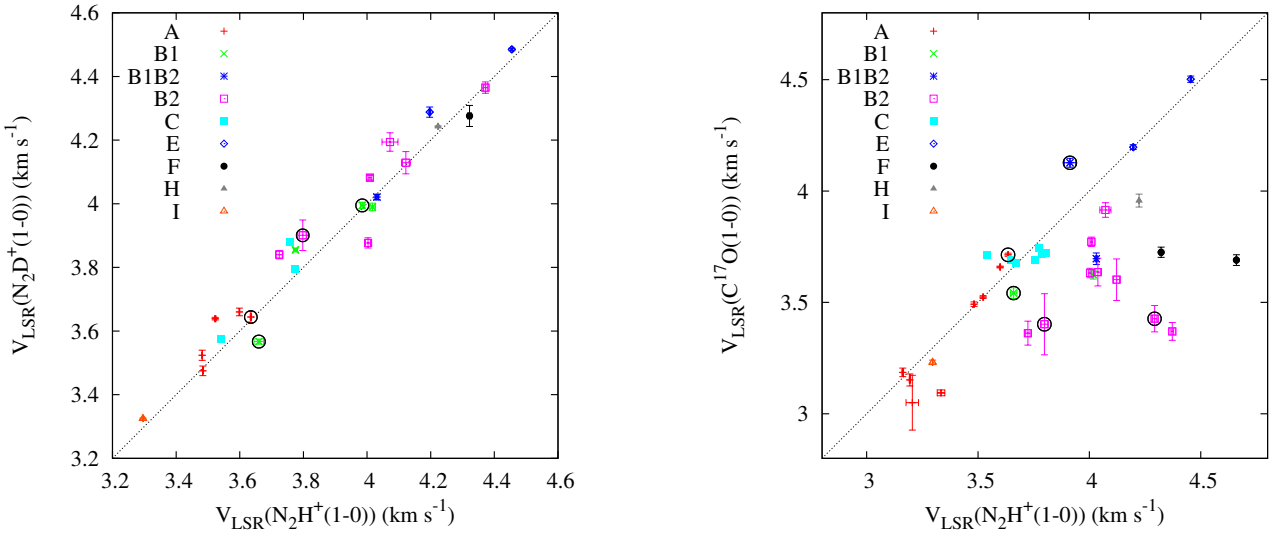

Fig. 3. V_{LSR} of N_2D^+(1–0) on the left panel and $C^{17}O$(1–0) on the right panel as a function of the V_{LSR} of the N_2H^+(1–0) line. Black dotted lines are the lines of equal V_{LSR}. The protostellar cores are marked with black open circles.

.

and $C^{17}O$ line widths, we took the Δv of the component having the closest V_{LSR}.

The N_2H^+ and N_2D^+ (1–0) line widths range from 0.2 to 0.7 km s^{-1}, except for the blended N_2D^+ line at B2-MM8 (1.2 km s^{-1}, see left panel of Fig. 5). While the line widths of the N_2H^+ and N_2D^+ (1–0) lines are similar for most of the cores, 84% of the cores are within 0.1 km s^{-1} of each other, the $C^{17}O$(1–0) line widths are overall larger than those of N_2H^+(1–0). The median width difference is 0.38 km s^{-1} and the median line width ratio is 1.9. Similar to what was found with the line centroids, this suggests that the N_2H^+ and N_2D^+ trace the same gas, while $C^{17}O$ traces different, in particular more turbulent, gas.

3.2. Non-thermal motions

Figure 6 presents the ratio of non-thermal components Δv_{NT} of the N_2D^+(1-0), N_2H^+(1-0) and $C^{17}O$(1-0) lines and thermal line widths of a mean particle, Δv_T. The non-thermal components are derived from the observed line widths Δv_{obs} via:

$$\Delta v_{NT}^2 = \Delta v_{obs}^2 - 8\ln(2)\frac{kT_k}{m_{obs}}, \quad (1)$$

where k is Boltzmann's constant, T_k is the kinetic temperature, and m_{obs} is the mass of the observed molecule (Myers et al. 1991). To measure the non-thermal component, we use the kinetic temperature determined by Friesen et al. (2009) from ammonia observations. For those cores which were not observed in Friesen et al. (2009), we use dust temperatures determined by Pattle et al. (2015), assuming that the dust and gas tempera-

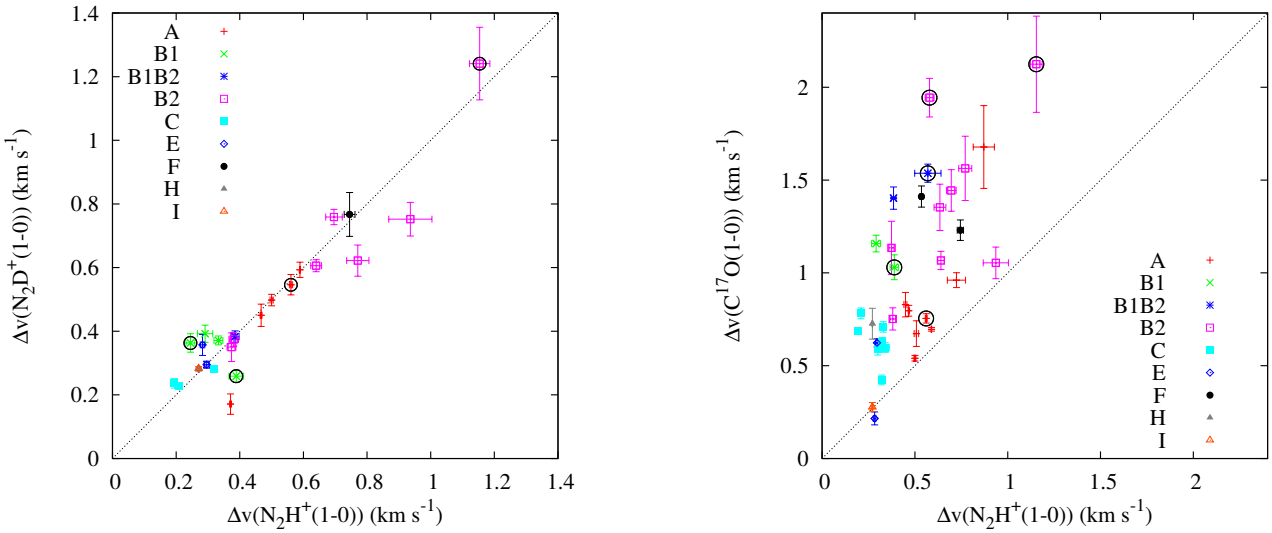

Fig. 5. Line widths, Δv, of N_2D^+(1–0) on the left panel and $C^{17}O$(1–0) on the right panel in comparison with Δv of N_2H^+(1–0). Black dotted lines are the lines of equal Δv. Different colors show different parts of the cloud. The protostellar cores are marked with black open circles.

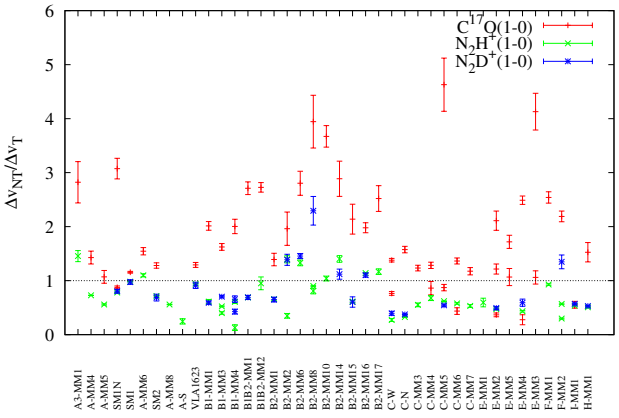

Fig. 6. Ratio of non-thermal components to thermal components of the N_2D^+(1–0), N_2H^+(1–0) and $C^{17}O$(1–0) lines. The dashed line shows the ratio equal to 1.

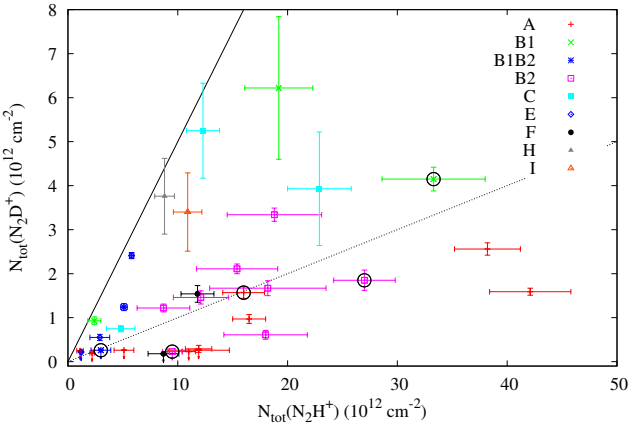

Fig. 7. Column densities of N_2D^+ and N_2H^+ with lines of constant deuterium fraction (R_D). The black line shows R_D=0.5 and the dotted line shows R_D=0.1. The protostellar cores are depicted with black open circles.

tures are equivalent (assumption valid at volume densities above 10^4 cm^{-3}; Goldsmith 2001). For most of the cores where both the gas and dust temperatures have been measured, the two values are indeed similar, with the only exception being the B2 region, where the dust temperature is a few degrees lower than the gas temperature. This may be due to the effect of protostellar feedback, where shocks produced by outflows entraining the dense gas can heat the gas but not the dust (e.g. Draine 1980). For the I-MM1 core neither dust nor gas temperatures have ever been estimated, so we adopt 11 K, the same as H-MM1, as these two cores have similar characteristics, both being relatively isolated and far away from the main source of irradiation and heating (see Section 4.5). The kinetic temperatures for all cores are given in Table A.7.

For typical temperatures of 10–20 K across L1688, the thermal line widths, Δv_T, for a mean particle with mass 2.33 amu are 0.44–0.63 km s^{-1}. The majority of $C^{17}O$(1–0) lines are supersonic (78%) while most of N_2H^+(1–0) and N_2D^+(1–0) lines are subsonic (80% and 75%). The non-thermal to thermal line width ratio can be as high as 1.5 for N_2H^+(1–0), 2.5 for N_2D^+(1–0), and as high as 5 for $C^{17}O$(1–0). The most turbulent region is Oph-B2 and the most quiescent regions are Oph-B1, C, E, H and I. Oph-A contains turbulent as well as relatively quiescent cores. For most cores, N_2D^+(1–0) and N_2H^+(1–0) have similar non-thermal components and are narrower than the $C^{17}O$(1–0) line.

3.3. Column densities and deuterium fractions

The hfs fits provide values needed to measure the excitation temperature (T_{ex}) and its error. These values are: the total optical depth, i.e. the sum of the optical depths of the various hyperfine components (τ), the quantity labelled $T_{ant}\times\tau$ (see below), the full width at half maximum of the line (FWHM, Δv) and the centroid velocity relative to the local standard of rest (V_{LSR}). In case of optically thick lines, $T_{ant} \times \tau$ is the total optical depth times the difference between the Rayleigh-Jeans equivalent excitation and

background temperatures, while for optically thin lines it is the main beam temperature (T_{mb}). The T_{ex} can be calculated as

$$T_{ex} = \frac{h\nu}{k}\left[\ln\left(\frac{h\nu/k}{(T_{ant}\times\tau)/\tau + J_\nu(T_{bg})} + 1\right)\right]^{-1}, \quad (2)$$

where h is the Planck constant, k is the Boltzmann constant, ν is the frequency of the observed transition, T_{bg} is the cosmic background temperature (2.7 K), $J_\nu(T_{bg})$ is the equivalent Rayleigh-Jeans background temperature, and $J_\nu(T)$ is the function

$$J_\nu(T) = \frac{h\nu/k}{\exp(h\nu/kT) - 1}. \quad (3)$$

The calculated excitation temperature depends on the value of τ. In the case of weak lines or low S/N, τ can not be determined properly and the error of τ ($\Delta\tau$) will be high. In all cases where $\tau/\Delta\tau \leq 3$, we consider the lines to be optically thin and fix $\tau = 0.1$ (the minimum opacity value) in CLASS. In this case of optically thin conditions, for $N_2H^+(1-0)$, the excitation temperature value is assumed to be the average T_{ex} found for optically thick $N_2H^+(1-0)$ lines, while for $N_2D^+(1-0)$ we adopt the (measured or assumed) $N_2H^+(1-0)$ excitation temperature toward the same dense core.

For optically thick transitions, the column density (N_{tot}) is given by:

$$N_{tot} = \frac{8\pi^{3/2}\Delta\mathrm{v}}{2\sqrt{\ln 2}\lambda^3 A_{ul}}\frac{g_l}{g_u}\frac{\tau}{1-\exp(-h\nu/kT_{ex})}\frac{Q_{rot}}{g_l\exp(-E_l/kT_{ex})}, \quad (4)$$

where λ is the wavelength of the observed transition, A_{ul} is the Einstein coefficient of the $u \rightarrow l$ transition, g_l and g_u are the statistical weights of the lower and upper levels, Q_{rot} is the partition function and E_l is the energy of the lower level (Caselli et al. 2002b). For linear rotors, g_l and g_u are determined by $g_J = 2J+1$, where J is the rotational quantum number. The partition function of linear molecules (such as N_2H^+ and CO) is given by

$$Q_{rot} = \sum_{J=0}^{\infty}(2J+1)\exp(-E_J/kT), \quad (5)$$

where $E_J = J(J+1)hB$, and B is the rotational constant. For rotational transitions with hyperfine structure, τ refers to the total optical depth (given by the sum of the peak optical depths of all the hyperfine components) and Δv to the intrinsic line width. The error on N_{tot} is given by propagating the errors on Δv, τ and T_{ex} in equation 4.

For optically thin lines

$$N_{tot} = \frac{8\pi W}{\lambda^3 A_{ul}}\frac{g_l}{g_u}\frac{1}{J_\nu(T_{ex}) - J_\nu(T_{bg})}\frac{1}{1-\exp(-h\nu/kT_{ex})}\times \times\frac{Q_{rot}}{g_l\exp(-E_l/kT_{ex})}, \quad (6)$$

where W is the integrated intensity of the line:

$$W = \frac{\sqrt{\pi}\Delta\nu T_{mb}}{2\sqrt{\ln 2}}, \quad (7)$$

for a Gaussian line (Caselli et al. 2002b).

In case of non-detection of N_2D^+, upper limits on the N_2D^+ column density have been derived based on the 3σ uncertainty ($3\,\sigma_W$) of the integrated intensity, with:

$$\sigma_W = rms \times \sqrt{N_{ch}} \times \Delta\mathrm{v_{res}}, \quad (8)$$

where N_{ch} is the mean number of channels covering the velocity range of all the detected lines and $\Delta\mathrm{v_{res}}$ is the velocity resolution.

The column densities of N_2H^+, N_2D^+ and $C^{17}O$ are given in tables A.2–A.6. The N_2D^+ column densities derived from the (1–0) transition in most cores are larger than those derived from the (2–1) transition on average by only 10%. $C^{17}O$ column densities calculated with (1–0) lines in most cores are smaller than the ones calculated with (2–1) lines (see section 3.4 for details). Figure 7 shows the column densities of N_2H^+ and N_2D^+. Where multiple components are detected, we plot the sum of the column densities.

The deuterium fraction is defined as the ratio of column densities, $R_D = N_{tot}(N_2D^+)/N_{tot}(N_2H^+)$, and it has been measured for all cores where the $N_2D^+(1-0)$ line is detected. To calculate the deuterium fraction for cores where two velocity components are detected, we take the sum of the column densities derived from the two components. L1688 overall exhibits high levels of deuterium fractions with a large spread of values between different cores (R_D = 2–76 %; see Fig. 8). Such a high level of deuteration (over 20 %) was previously found toward other dense cores in different star forming regions (e.g. Crapsi et al. 2005; Pagani et al. 2007; Emprechtinger et al. 2009; Fontani et al. 2011; Miettinen et al. 2012; Friesen et al. 2013; Fontani et al. 2014). The deuterium fraction across the B2 region was previously studied by Friesen et al. (2010), who found slightly lower deuterium fractions (1–10%) than in the present work (3–18%). The column densities of N_2D^+ (0.5–6$\times10^{11}$ cm^{-2}) and N_2H^+ (4–10$\times10^{12}$ cm^{-2}) they obtain are also smaller than those found in this work (6–33$\times10^{11}$ and 9–27$\times10^{12}$ cm^{-2}). This difference could be due to different transitions used to calculate column densities, while using similar excitation temperatures derived from the N_2H^+(1–0) line. Friesen et al. (2010) used N_2D^+(3–2) and N_2H^+(4–3) lines with 11″ and 13″ HBPW while we use the (1–0) transition for both species (32″ and 27″). The factor of 2 difference in deuterium fraction could arise also from not coincident dense core coordinates.

3.4. CO-depletion factor

In cold, dense, quiescent gas, CO freezes out onto dust grains and the level of this depletion is commonly expressed as a CO-depletion factor, f_d, calculated as:

$$f_d = \frac{X_{ref}(\mathrm{CO})}{X(\mathrm{CO})}, \quad (9)$$

where X_{ref}(CO) is the reference abundance and X(CO) is the observed abundance.

The reference abundance of CO in the local ISM has been found to be between 1 and 2$\times10^{-4}$ (Wannier 1980; Frerking et al. 1982; Lacy et al. 1994). We use $X_{ref}(C^{16}O) = 2\times10^{-4}$ (Frerking et al. 1982), $X(C^{18}O)/X(C^{17}O) = 4.11$ (Wouterloot et al. 2005) and $X(C^{16}O)/X(C^{18}O) = 560$ (Wilson & Rood 1994) such that:

$$X(C^{16}O) = \frac{N_{tot}(C^{17}O)\times 4.11\times 560}{N(H_2)}. \quad (10)$$

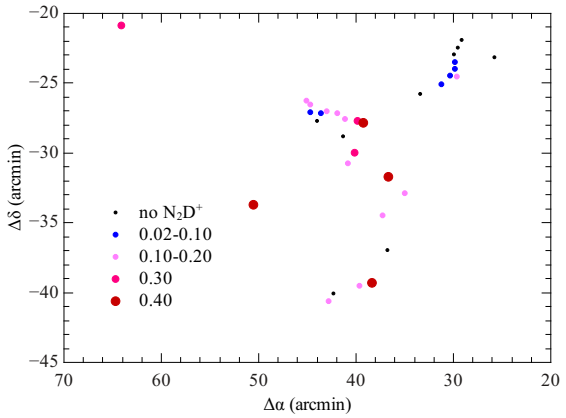

Fig. 8. Deuterium fraction across L1688. The black points show the cores with no $N_2D^+(1–0)$ detection. The coordinate offsets correspond to the J2000 equatorial position $\alpha = 16^h24^m16^s$, $\delta = -24°00'00''$.

To calculate the f_d in case of multiple velocity components, we consider the sum of the column densities of the individual components (as $N(H_2)$ is derived from the millimetre dust continuum emission, which does not contain kinematic information). Since millimetre dust continuum emission is generally optically thin, the molecular hydrogen column density can be derived from the continuum flux density:

$$N(H_2) = \frac{S_\lambda}{\Omega \mu_{H_2} m_H \kappa_\lambda B_\lambda(T_{dust})}; \quad (11)$$

where S_λ is the flux in a single beam, Ω is the main beam solid angle, $\mu_{H_2} = 2.8$ is the mean molecular weight per H_2 molecule (Kauffmann et al. 2008), m_H is the mass of atomic hydrogen, κ_λ is the dust opacity per unit mass column density at a given wavelength ($\kappa_{850\mu m}$=0.01 cm^2 g^{-1}; Johnstone et al. 2000) and $B_\lambda(T_{dust})$ is the Planck function for a dust temperature T_{dust} (Motte et al. 1998).

The 850 μm dust continuum emission flux measurements from the SCUBA survey (with the beam size of the convolved map of 22″.9, Di Francesco et al. 2008) have been used to calculate $N(H_2)$, adopting the dust temperature from Pattle et al. (2015) when available and the gas temperature from Friesen et al. (2009) in the other cases. For those cores not studied in the above mentioned papers, the dust temperature estimated by Motte et al. (1998) has been adopted. For Oph-I, where no dust or gas temperature has been measured, we assumed 11 K, the same as in Oph-H, as Oph-I has similar characteristics to Oph-H, as already mentioned. The dust temperatures for all cores are given in Table A.7.

The depletion factor of CO is generally quite low in L1688, ranging from 0.2 to 2 in the B1, B1B2, C, E, and F regions, and from to 0.7 to 7.3 in the A, B2, H and I regions. This result is consistent with previous large scale (e.g. Christie et al. 2012) and small scale (e.g. Bacmann et al. 2002; Gurney et al. 2008) studies. However, larger CO depletion factors are found for the A region compared to the work of Gurney et al. (2008): 1 to 6 instead of 1.5 to 4.5. This small discrepancy could be due to slightly different pointings or from the use of different CO isotopologues and transitions. In particular, we note that our $C^{17}O(2–1)$ observations tend to produce column densities larger than $N_{tot}(C^{17}O(1–0))$ by an average factor of 1.5 in Oph-A and 1.1 in B1, B1B2, B2, C, E and F regions (and thus depletion factors would be lower by 1.5 and 1.1), suggesting that temperature and density gradients along the line of sight may be present, slightly affecting the derived depletion factor depending on the CO transition used. To calculate column densities of $C^{17}O$, LTE is assumed, with the kinetic temperature equal to the dust temperature.

Christie et al. (2012) suggest that the low depletion factor of L1688 could be due to an unusual dust grain size distribution with a population of very large dust grains and very small spinning dust grains which reduces the surface area available for freeze-out. However, L1688 is a complex region, with active star formation and externally irradiated. Below, we discuss possible causes of the general low CO depletion factors and the significant variation in R_D and f_d found across L1688.

4. Discussion

4.1. Deuterium fraction

This work has found a large range of deuterium fractions across L1688, from a minimum of 2% to a maximum of 43%. Previous studies of deuterium fraction did not show such a big spread: for example, 5–25% in Taurus (Crapsi et al. 2005), 1–10% in Ophiuchus B (Friesen et al. 2010), and 3–25% in Perseus (Emprechtinger et al. 2009; Friesen et al. 2013). The large values of deuterium fractions found toward some of the cores in L1688 in our more extensive survey may indicate the presence of centrally concentrated pre-stellar cores on the verge of star formation. The Ophiuchus Molecular Cloud is known to be denser on average than other nearby star forming regions (e.g. Lada et al. 2013). The higher average densities, together with the generally higher molecular cloud temperatures (Pattle et al. 2015; Liseau et al. 2015), imply larger pressures which may accelerate the formation of denser cores and the rate of star formation (e.g. Kennicutt & Evans 2012) compared to the other nearby molecular cloud complexes. It is interesting to note that these high R_D values are found toward E-MM2d, C-Ne, I-MM1, H-MM1, B1-MM1, B1-MM3, B1B2-MM1 which do not prominently appear in the 850 μm map and they are all relatively isolated structures (I and H) or in between bright sub-millimetre clumps (E, C-N, B1, B1B2). They are probably recently formed cold and dense structures on the verge of star formation.

4.2. Deuterium fraction and CO depletion

Deuterium fraction and CO-depletion factor are expected to correlate, because CO is one of the main destruction partners of H_3^+ and its deuterated forms (Dalgarno & Lepp 1984). This correlation has been presented in several theoretical works (Crapsi et al. 2005; Caselli et al. 2008; Kong et al. 2015) and confirmed with observations (Crapsi et al. 2005; Emprechtinger et al. 2009; Friesen et al. 2013). Figure 9 shows the deuterium fraction as a function of CO-depletion factor in L1688. The dotted curve on the figure shows the prediction from simple modelling by Crapsi et al. (2005), shifted to take into account the different reference CO abundance adopted here. The first thing to note is that f_d values go below 1, which suggests that our adopted X_{ref}(CO) has been underestimated by a factor of a few (2–3, considering the lowest f_d value in Table A.7); or the dust opacity, κ, which depends on the evolutionary stage and the properties of dust grains (see Henning et al. 1995) has been overestimated by a factor of 1.5–2, or the dust temperature has been overestimated by a few (1–3) K. However, to allow comparison with recent literature work (where $X_{ref}(CO) = 2\times10^{-4}$, see e.g. Hernandez et al.

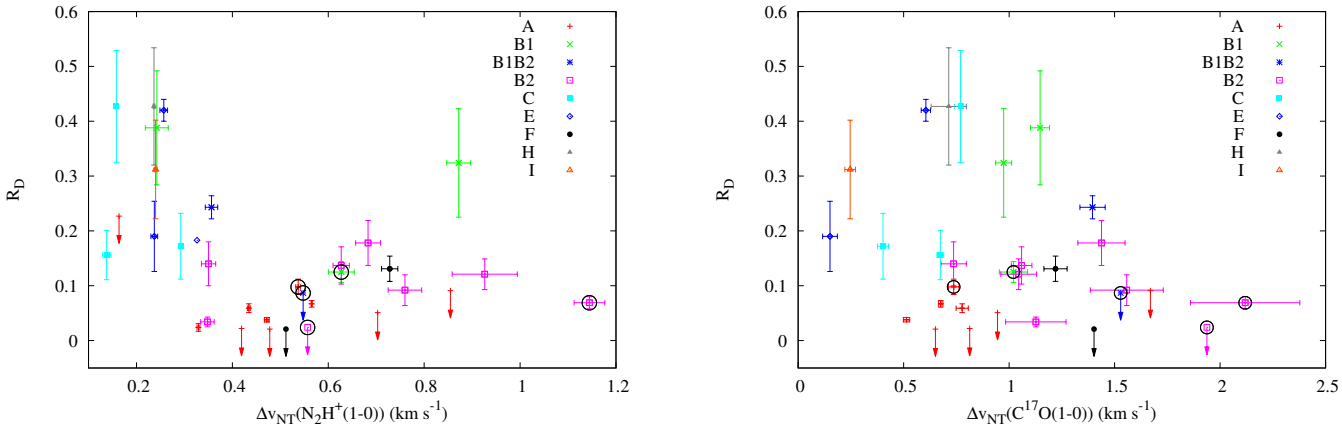

Fig. 10. Deuterium fraction as a function of the nonthermal component of the N_2H^+(1–0) line width (left) and the $C^{17}O$(1–0) line width (right). The protostellar cores are depicted with black open circles.

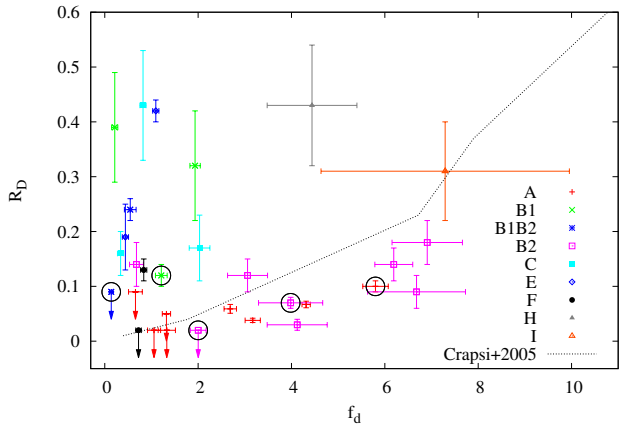

Fig. 9. Deuterium fraction as a function of CO-depletion factor. The protostellar cores are depicted with black open circles.

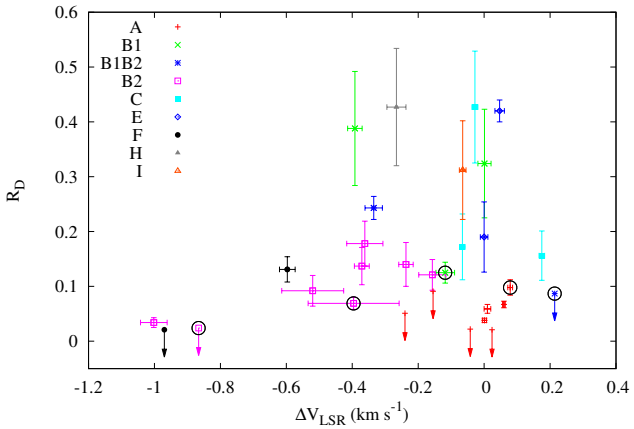

Fig. 11. Deuterium fraction as a function of the difference between the central velocities of the $C^{17}O$(1–0) and N_2H^+(1–0) lines ΔV_{LSR}. The protostellar cores are depicted with black open circles.

2011; Fontani et al. 2012), and considering the factor of 2 uncertainty associated with X_{ref}(CO) (see also Miotello et al. 2014), we did not modify X_{ref}(CO), warning the reader that the calculated f_d values may be underestimated by a factor of a few. The important message here is to see if previously found trends are reproduced and/or if L1688 hosts dense cores with a larger variety of chemical/physical properties than found in other nearby star forming regions.

From Fig. 9, it is evident that two classes of cores are present in L1688. One group includes the A, B2 and I cores, which show a correlation between R_D and f_d similar to that found by Crapsi et al. (2005). The other group contains the B1, B1B2, C, E, F and H cores, which completely deviate from the Crapsi et al. (2005) correlation. This latter group of cores shows R_D =12–43% and f_d =0.2–4.4. From the parameter space exploration of Caselli et al. (2008) and Kong et al. (2015), large values of R_D (> 0.02) cannot be achieved in standard conditions if little CO freeze-out is present *in the same gas traced by* N_2D^+. How to reconcile theory with observations? One possibility is that the dense and cold regions responsible for the bright N_2D^+ lines have sizes smaller than the IRAM-30m beam at 3mm. In this case, the CO-depleted zone would be too diluted to be clearly detected within the larger scale CO-emitting region. Indeed, 2 of 6 cores with R_D > 20% and f_d < 4.4 (B1-MM3 and B1B2-MM1) have estimated sizes 1300–1800 AU, less then 2640 AU corresponding to 22″ at 120 pc, one unresolved (B1-MM1) (Motte et al. 1998), one (H-MM1) has no size estimate (outside of the mapped area in Motte et al. 1998). Higher angular resolution observations of dust continuum and molecular lines are needed to prove this point.

4.3. Deuterium fraction and non-thermal motions

To understand further the characteristics of the highly deuterated, but CO-rich cores in Fig. 9, we plot the deuterium fraction as a function of non-thermal line width of N_2H^+(1–0) and $C^{17}O$(1–0) in Fig. 10. This figure shows that these cores preferentially occupy the left area of the panels, indicating that on average they have narrower $C^{17}O$(1–0) and especially N_2H^+(1–0) lines. Thus, the highly deuterated cores are overall more quiescent than the rest of the sample, in agreement with their relatively isolated nature and maybe smaller size, as mentioned in the previous section. Please also note that these are the cores with relatively small differences between $C^{17}O$(1–0) and N_2H^+(1–0) LSR velocities (see Fig. 11), again suggesting quiescent conditions. The rest of the sample displays broader line-widths, suggestive of faster internal motions (in case of gravitational contraction) or external stirring, e.g. due to proximity to active sites of star formation. Indeed, relatively large N_2H^+(1–0) line widths

have been found by Crapsi et al. (2005) toward some of the most evolved starless cores in their sample (L1544 and L429; see their Fig. 6). Line widths tend to increase toward the centre of L1544 (Caselli et al. 2002a) because of contraction motions. The quiescent and highly deuterated cores found in L1688 may then represent an earlier evolutionary stage, compared to L1544 and other contracting pre-stellar cores, where the core has just started to become centrally concentrated but contraction has not started yet (or it has not affected scales large enough to be detected with the current single-dish observations). High angular resolution observations are needed to investigate this conclusion.

4.4. R_D and f_d versus molecular hydrogen column density and temperature

The measured R_D and f_d values are plotted as a function of molecular hydrogen column density, $N(H_2)$, and dust temperature, T_{dust}, in Fig. 12. No correlation is found for R_D vs $N(H_2)$, while f_d appears to increase with $N(H_2)$ with different slopes depending on the region. In particular, f_d is increasing faster with $N(H_2)$ in the B2 region compared to the A and C regions. For the other regions, it is hard to see any trend, probably because of the more limited range of $N(H_2)$ values detected. One possible cause of the different slopes in the f_d – $N(H_2)$ correlations is the different amount of external heating due to the proximity of Oph-A to HD 147889 (see next section and Fig. 13). This extra illumination maintains the dust grains in region A at a higher temperature compared to the other L1688 regions (see also Liseau et al. 2015), so that larger column/volume densities are needed to reach dust temperatures low enough (<25 K) to allow CO molecules to freeze-out onto the dust grains. The C region which rather follow the same trend as the A region is the next close to HD 147889 after the A region (see Fig. 13) and probably also illuminated by the star, although it's temperature ($\leq$ 15 K) and column density ($\leq 10^{22}$ cm^{-2}) are as low as in the other regions.

The difference in dust temperatures among the various regions in L1688 is also causing the scatter plot in the right panels of Fig. 12. Here we note that the different amount of external illumination impinging the different L1688 regions causes the well-known f_d vs T_{dust} correlation (e.g. Kramer et al. 1999) to disappear. Oph-A is the only region in L1688 with dust temperatures larger than 15 K and significant CO freeze-out. Oph-B2 displays a sharp drop of f_d with increasing T_{dust}, as expected given the exponential dependence on T_{dust} of the CO evaporation rate (see e.g. Hasegawa et al. 1992).

The deuterium fraction is also expected (and has been measured) to drop with dust temperatures above about 15-20 K (.e.g. Emprechtinger et al. 2009; Caselli et al. 2008; Kong et al. 2015). However, this trend is not observed in L1688, as shown in the top left panel of Fig. 12. Once again, the non-uniform conditions among the various regions (in particular the amount of external illumination, gas volume density etc.) make it difficult to see a well defined pattern. Even within the same regions, we do not notice any trend, which may be caused by dust temperatures (mainly derived from Herschel data) not being representative of the cold regions within which the deuterium fractionation is taking place. More detailed and higher resolution data are needed to explore this possibility.

4.5. Distance to heating sources

It is well-known that star formation in L1688 is affected by the OB-association Sco OB 2 (Pattle et al. 2015), which is located ~11 pc behind L1688 (Mamajek 2008). Sco OB 2 is a moving group of more than 120 stars, mostly of B and A spectral types. It occupies an area of about 15° diameter on the sky (de Zeeuw et al. 1999). We looked for a correlation between R_D, f_d, the distance to nearby stars (ρ Oph, HD 147889, V 2246 Oph, Oph S1) and the closest YSOs (see Fig. 13). ρ Oph is a multiple system of B2IV–B2V spectral type stars; it is a member of the Sco OB 2 association, located to the North of L1688, and is the most distant from L1688 among the four nearby stars. The cores in Oph-A, the nearest region to ρ Oph, show a correlation between the CO-depletion factor and the projected angular distance D to the ρ Oph system, with f_d increasing with D (see Fig. 14). The cores in the others sub-regions do not show any correlation.

The other three stars are pre-main sequence stars related to the Ophiuchus star-forming region. Oph S1 is a B4-K8 type binary star with a T-Tauri star being the fainter component (Gagné et al. 2004) to the East of the A region; V 2246 Oph is a Herbig Ae/Be star on the West side of the A region; and HD 147889 is a pre-main sequence star on the West side of L1688. In all regions of L1688, f_d does not show any correlation with the distance to the brightest PMS stars of L1688.

The A region contains more YSOs than other regions and is the closest to the external heating sources. Oph-A has the smallest values of R_D and the highest values of f_d in L1688. Relatively low deuteration could be due to this proximity to nearby irradiating sources, while the large f_d values may be due to the fact that this region is also the densest one in L1688, thus probably harbouring the densest cores. Here, the dust temperatures are probably low enough (< 25 K) to allow molecular freeze-out to proceed at a higher rate due to the larger gas-dust collision rates (because of the overall larger densities), but not large enough to promote deuterium fractionation, likely because of an increase of the ortho-to-para H_2 ratio in warmer environments (see e.g. Flower et al. 2006). An alternative to the low values of R_D found in Oph-A could be that N_2D^+ cores are compact and small compared to our beam, while N_2H^+ is extended and abundant due to the large average densities (see e.g. Friesen et al. 2014; Liseau et al. 2015), as also found in Infrared Dark Clouds where massive stars and star clusters form (Henshaw et al. 2014). Indeed, Friesen et al. (2014) detected compact (a few hundred AU in size) dust continuum condensation and ortho-H_2D^+ emission toward one of the cores embedded in Oph-A. However, we note that the line widths of N_2H^+(1–0) and N_2D^+(1–0) lines are the same within the errors (see Fig. 5), so this alternative scenario may be harder to justify. Again, higher angular resolution observations of N_2D^+ are needed to disentangle between these two scenarios.

No correlation between R_D and distance to any heating source (embedded or external) was found, although the largest R_D values are found at projected distances larger than 50 arcsec from embedded YSOs and greater than 20 arcsec from HD 147889 (these are the already discussed large R_D - low f_d relatively isolated cores, which we discussed in section 4.2). Moreover, the region closest to ρ Oph and V 2246 Oph, the sub-region Oph-A, has the lowest deuterium fractions.

Friesen et al. (2010) studied the deuterium fraction in the B2 region and found a correlation between R_D and distance to the nearest protostar. The deuterium fraction we measure in this region (0–18%, median ~12%) is systematically higher than that found by Friesen et al. (2010) (0–10%, mostly < 4%). According

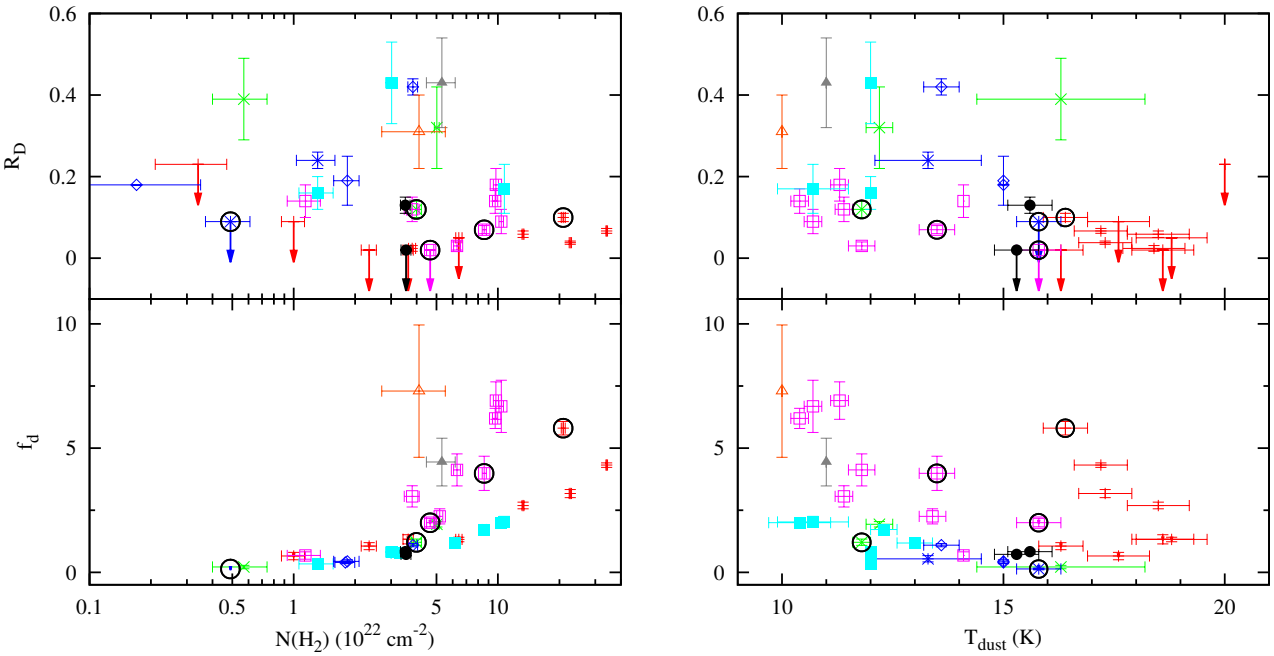

Fig. 12. Left upper panel: deuterium fraction depending on the molecular hydrogen column density, $N(H_2)$. Right upper panel: deuterium fraction as a function of dust temperature taken from Pattle et al. (2015); Friesen et al. (2009) and Motte et al. (1998). Left lower panel: CO-depletion factor versus the molecular hydrogen column density. Right panel: CO-depletion factor as a function of dust temperature. The protostellar cores are depicted with black open circles, the color coding is given in Fig. 11.

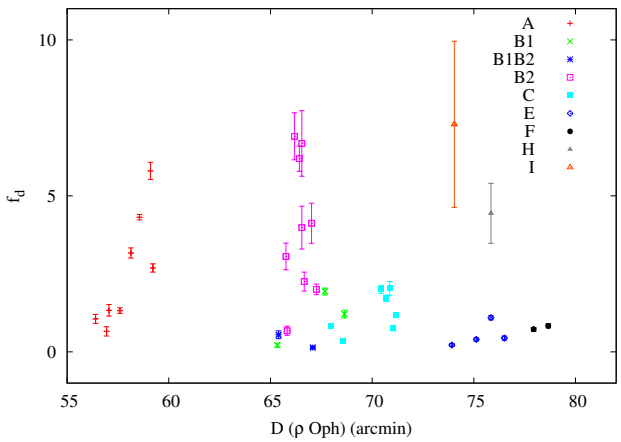

Fig. 14. CO-depletion factor as a function of angular distance to the ρ Oph system.

to our study, there is no correlation between R_D and the distance to the closest YSO (see Fig. 13 right upper panel). This difference in the results of the studies (R_D — YSO correlation) can be due to the fewer cores studied by us in this particular region (9 cores instead of full mapping of the B2 region as done by Friesen et al. 2010).

5. Conclusions

This paper presents single point observations of the ground state transitions of N_2H^+, N_2D^+ and $C^{17}O$ toward prestellar cores in L1688. We measure the deuterium fraction, R_D, and CO-depletion factor, f_d, and study the correlation between these two parameters as well as with physical parameters varying across the cloud, such as dust temperature, molecular hydrogen column density, level of turbulence, projected distance to stellar sources which externally irradiate the cloud and embedded sources which can internally stir and shock the gas. The following conclusions have been reached:

1. The L1688 cores show a large spread of deuterium fractions, 2–43% and moderate CO depletion factors (up to 7, although the reference value of the CO fractional abundance adopted here, 2×10^{-4}, may be underestimated by a factor of 2–3 or the dust opacity value used in the work, 0.01 cm^2 g^{-1} may be overestimated by a factor of 1.5–2).
2. The largest R_D values are found toward (B1, B1B2, C, E, H, I) dense cores which present relatively quiescent (subsonic) motions as measured from the width of the high density tracer lines; thus, they are probably in an evolutionary stage just preceding the contraction toward protostellar birth, as found in other more evolved pre-stellar cores such as L1544 in Taurus (Caselli et al. 2002a). These highly deuterated cores are also relatively isolated (they are typically found in between strong sub-millimetre dust continuum emission

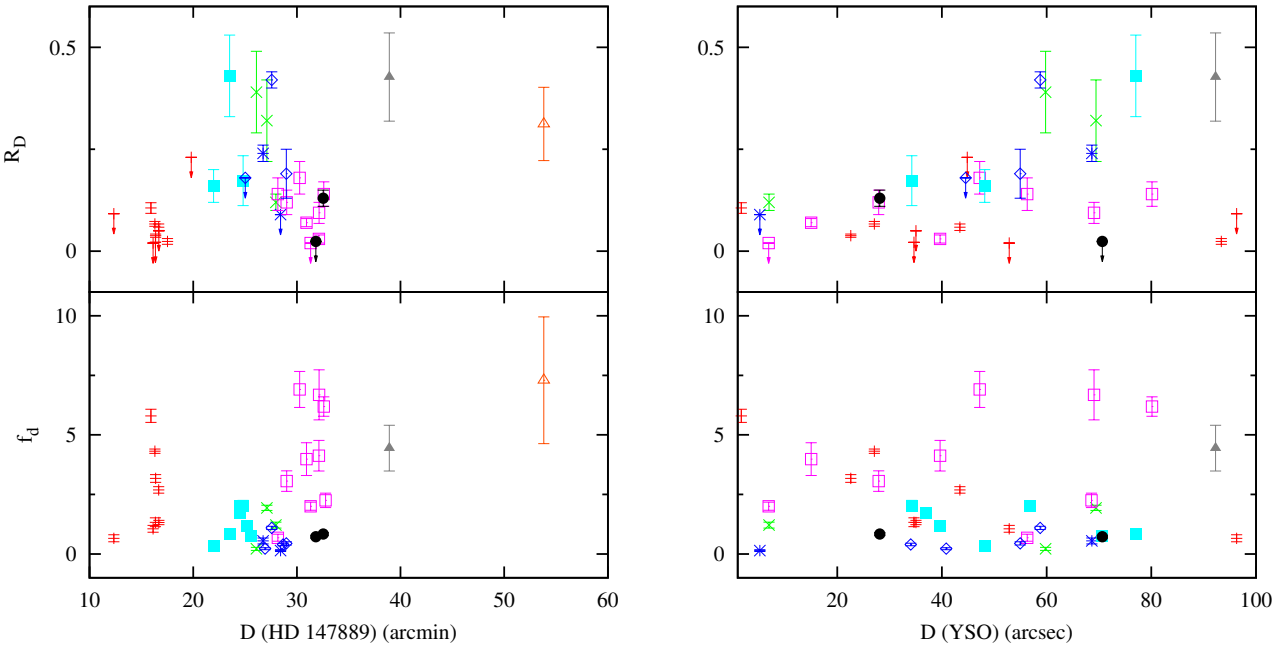

Fig. 13. Left upper panel: deuterium fraction depending on the angular distance to HD 147889. Right upper panel: deuterium fraction as a function of the angular distance to the closest YSO. The positions of YSOs were taken from Motte et al. (1998); Simpson et al. (2008) and Dunham et al. (2015). Left lower pannel: CO-depletion factor depending on the angular distance to HD 147889. Right lower panel: CO-depletion factor depending on the angular distance to the closest YSO. The color coding is given in Fig. 11.

and far away from embedded protostars) and the CO freeze-out is low, in contrast with chemical model predictions. This dichotomy (large R_D and low f_d) can be understood if the deuterated gas is confined in a region smaller than the beam size, so that the CO-depleted region is too small to be revealed with observations of the widespread $C^{17}O$(1–0) emitting gas. Higher angular resolution observations are needed to confirm this statement.

3. Except for this sub-group of highly deuterated cores, widths are generally supersonic in $C^{17}O$(1–0) (78%) and subsonic in N_2H^+(1–0) and N_2H^+(1–0) (75% and 80%). The B2 region stands out here with supersonic widths in all tracers in the majority of cores. This is probably a combination of internal systematic motions (e.g. contraction) and external stirring (turbulence, interaction with outflow driven by embedded protostars).
4. The correlation between R_D and f_d already found in other studies of starless cores is maintained for a sub-group of cores (those in A, B2 and I, when plotted together). The highly deuterated cores show a significantly steeper rise of R_D with f_d, suggesting that the CO observations are not sensitive to the CO-depleted zone, as mentioned above.
5. The densest region in L1688, Oph-A, hosts dense cores with significant amount of CO freeze-out (f_d close to 7) but no corresponding large R_D values. This can be explained if the gas and dust temperatures are low enough (<25 K) to allow CO freeze-out but high enough to significantly increase the ortho-to-para ratio compared to cooler regions. Alternatively, the N_2D^+ cores may be small and diluted within our beam, whereas the N_2H^+ is abundant all across the region as a consequence of the large average densities.
6. The nearby ρ Oph star in the Sco OB2 association appears to affect the amount of CO freeze-out in Oph-A cores, as f_d increases with projected distance to this star. No other regions appear to be chemically affected by their proximity to external stars or embedded young stellar objects, except for the B2 region, where f_d decreases with increasing dust temperature.
7. Our observations hint at the present of compact starless cores (smaller than those found toward less dense and cooler molecular cloud complexes, such as Taurus) with large deuterium fractions (12–43%) and small CO depletion factors (0.2–4.4). These cores have relatively low temperatures compared to their surroundings, so that they do not appear as clear structures in dust continuum emission maps at 850 μm. Their compact nature may be a consequence of the overall higher densities and temperatures across L1688 compared to other nearby star forming regions. High angular resolution observations are needed to test these predictions.

Acknowledgements. The authors thank J. Pineda for thoughtful comments which helped to improve the manuscript. The authors acknowledge the financial support of the European Research Council (ERC; project PALs 320620); Andy Pon acknowledge that partial salary support was provided by a CITA National Fellowship.

References

André, P., Belloche, A., Motte, F., & Peretto, N. 2007, A&A, 472, 519
Bacmann, A., Lefloch, B., Ceccarelli, C., et al. 2002, A&A, 389, L6
Benson, P. J. & Myers, P. C. 1989, ApJS, 71, 89
Bergin, E. A. & Tafalla, M. 2007, ARA&A, 45, 339
Caselli, P. 2011, in IAU Symposium, Vol. 280, IAU Symposium, ed. J. Cernicharo & R. Bachiller, 19–32
Caselli, P. & Ceccarelli, C. 2012, A&A Rev., 20, 56
Caselli, P., Vastel, C., Ceccarelli, C., et al. 2008, A&A, 492, 703
Caselli, P., Walmsley, C. M., Tafalla, M., Dore, L., & Myers, P. C. 1999, ApJ, 523, L165
Caselli, P., Walmsley, C. M., Zucconi, A., et al. 2002a, ApJ, 565, 331
Caselli, P., Walmsley, C. M., Zucconi, A., et al. 2002b, ApJ, 565, 344
Christie, H., Viti, S., Yates, J., et al. 2012, MNRAS, 422, 968
Crapsi, A., Caselli, P., Walmsley, C. M., et al. 2005, ApJ, 619, 379
Dalgarno, A. & Lepp, S. 1984, ApJ, 287, L47
de Zeeuw, P. T., Hoogerwerf, R., de Bruijne, J. H. J., Brown, A. G. A., & Blaauw, A. 1999, AJ, 117, 354
di Francesco, J., Evans, II, N. J., Caselli, P., et al. 2007, Protostars and Planets V, 17
Di Francesco, J., Johnstone, D., Kirk, H., MacKenzie, T., & Ledwosinska, E. 2008, ApJS, 175, 277
Draine, B. T. 1980, ApJ, 241, 1021
Dunham, M. M., Allen, L. E., Evans, II, N. J., et al. 2015, ApJS, 220, 11
Emprechtinger, M., Caselli, P., Volgenau, N. H., Stutzki, J., & Wiedner, M. C. 2009, A&A, 493, 89
Flower, D. R., Pineau Des Forêts, G., & Walmsley, C. M. 2006, A&A, 449, 621
Fontani, F., Giannetti, A., Beltrán, M. T., et al. 2012, MNRAS, 423, 2342
Fontani, F., Palau, A., Caselli, P., et al. 2011, A&A, 529, L7
Fontani, F., Sakai, T., Furuya, K., et al. 2014, MNRAS, 440, 448
Frerking, M. A. & Langer, W. D. 1981, J. Chem. Phys., 74, 6990
Frerking, M. A., Langer, W. D., & Wilson, R. W. 1982, ApJ, 262, 590
Friesen, R. K., Di Francesco, J., Bourke, T. L., et al. 2014, ApJ, 797, 27
Friesen, R. K., Di Francesco, J., Myers, P. C., et al. 2010, ApJ, 718, 666
Friesen, R. K., Di Francesco, J., Shirley, Y. L., & Myers, P. C. 2009, ApJ, 697, 1457
Friesen, R. K., Kirk, H. M., & Shirley, Y. L. 2013, ApJ, 765, 59
Fuller, G. A. & Myers, P. C. 1992, ApJ, 384, 523
Gagné, M., Skinner, S. L., & Daniel, K. J. 2004, ApJ, 613, 393
Goldsmith, P. F. 2001, ApJ, 557, 736
Gurney, M., Plume, R., & Johnstone, D. 2008, PASP, 120, 1193
Hasegawa, T. I., Herbst, E., & Leung, C. M. 1992, ApJS, 82, 167
Henning, T., Michel, B., & Stognienko, R. 1995, Planet. Space Sci., 43, 1333
Henshaw, J. D., Caselli, P., Fontani, F., Jiménez-Serra, I., & Tan, J. C. 2014, MNRAS, 440, 2860
Herbst, E. & Klemperer, W. 1973, ApJ, 185, 505
Hernandez, A. K., Tan, J. C., Caselli, P., et al. 2011, ApJ, 738, 11
Johnstone, D., Wilson, C. D., Moriarty-Schieven, G., et al. 2000, ApJ, 545, 327
Kauffmann, J., Bertoldi, F., Bourke, T. L., Evans, II, N. J., & Lee, C. W. 2008, A&A, 487, 993
Kennicutt, R. C. & Evans, N. J. 2012, ARA&A, 50, 531
Keto, E. & Caselli, P. 2008, ApJ, 683, 238
Kong, S., Caselli, P., Tan, J. C., Wakelam, V., & Sipilä, O. 2015, ApJ, 804, 98
Kramer, C., Alves, J., Lada, C. J., et al. 1999, A&A, 342, 257
Lacy, J. H., Knacke, R., Geballe, T. R., & Tokunaga, A. T. 1994, ApJ, 428, L69
Lada, C. J., Lombardi, M., Roman-Zuniga, C., Forbrich, J., & Alves, J. F. 2013, ApJ, 778, 133
Lada, C. J., Muench, A. A., Rathborne, J., Alves, J. F., & Lombardi, M. 2008, ApJ, 672, 410
Linsky, J. L., Draine, B. T., Moos, H. W., et al. 2006, ApJ, 647, 1106
Liseau, R., Larsson, B., Lunttila, T., et al. 2015, A&A, 578, A131
Lombardi, M., Lada, C. J., & Alves, J. 2008, A&A, 480, 785
Mamajek, E. E. 2008, Astronomische Nachrichten, 329, 10
Miettinen, O., Harju, J., Haikala, L. K., & Juvela, M. 2012, A&A, 538, A137
Millar, T. J., Bennett, A., & Herbst, E. 1989, ApJ, 340, 906
Miotello, A., Bruderer, S., & van Dishoeck, E. F. 2014, A&A, 572, A96
Motte, F., Andre, P., & Neri, R. 1998, A&A, 336, 150
Myers, P. C., Ladd, E. F., & Fuller, G. A. 1991, ApJ, 372, L95
Pagani, L., Bacmann, A., Cabrit, S., & Vastel, C. 2007, A&A, 467, 179
Pagani, L., Daniel, F., & Dubernet, M.-L. 2009, A&A, 494, 719
Pagani, L., Salez, M., & Wannier, P. G. 1992, A&A, 258, 479
Pattle, K., Ward-Thompson, D., Kirk, J. M., et al. 2015, MNRAS, 450, 1094
Simpson, R. J., Nutter, D., & Ward-Thompson, D. 2008, MNRAS, 391, 205
Wannier, P. G. 1980, ARA&A, 18, 399
Ward-Thompson, D., Motte, F., & Andre, P. 1999, MNRAS, 305, 143
Wilson, T. L. & Rood, R. 1994, ARA&A, 32, 191
Wouterloot, J. G. A., Brand, J., & Henkel, C. 2005, A&A, 430, 549

Appendix A: Hyperfine splitting fit results

Please note that in tables A.2–A.6 the quantity labelled $T_{ant} \times \tau$, is $\tau \times (J_\nu(T_{ex}) - J_\nu(T_{bg}))$ in the case of optically thick transition ($\tau > 0.1$) or the main beam temperature (T_{mb}) in the case that the line is optically thin (with an adopted value of $\tau = 0.1$). For the details, see section 3.3.

Table A.1. Dense core coordinates and dataset numbers. Given coordinates are the observed positions, the centres of the cores determined by Motte et al. (1998).

Core	α_{J2000} (^{h} ^{m} ^{s})	δ_{J2000} ($^\circ$ $'$ $''$)	N_2H^+(1–0)	N_2D^+(1–0)	N_2D^+(2–1)	$C^{17}O$(1–0)	starless (s)/ protostellar (p)
			Dataset				
A3-MM1	16:26:09.7	-24:23:06	188-97	066-04	066-04	188-97	s
A-MM4	16:26:24.1	-24:21:52	188-97	066-04	066-04	188-97	s
A-MM5	16:26:25.9	-24:22:27	188-97	066-04	066-04	188-97	s
VLA1623	16:26:26.5	-24:24:31	188-97	066-04	066-04	188-97	p
SM1N	16:26:27.3	-24:23:28	188-97	066-04	066-04	188-97	s
SM1	16:26:27.5	-24:23:56	188-97	066-04	066-04	188-97	s
A-MM6	16:26:27.9	-24:22:53	188-97	066-04	066-04	188-97	s
SM2	16:26:29.5	-24:24:27	066-04	066-04	066-04	188-97	s
A-MM8	16:26:33.4	-24:25:01	066-04	066-04	066-04	–	s
A-S	16:26:43.1	-24:25:42	188-97	066-04	066-04	–	s
B1-MM1	16:27:08.7	-24:27:50	051-00	066-04	066-04	066-04	s
B1-MM3	16:27:12.4	-24:29:58	188-97	066-04	066-04	066-04	s
B1-MM4	16:27:15.7	-24:30:42	188-97	066-04	066-04	188-97	p
B1B2-MM1	16:27:11.3	-24:27:39	051-00	066-04	066-04	066-04	s
B1B2-MM2e	16:27:18.0	-24:28:48	051-00	066-04	–	066-04	p
B2-MM1	16:27:17.0	-24:27:32	051-00	066-04	066-04	066-04	s
B2-MM2	16:27:20.3	-24:27:08	051-00	066-04	066-04	066-04	s
B2-MM6	16:27:25.3	-24:27:00	188-97	066-04	066-04	066-04	s
B2-MM8	16:27:28.0	-24:27:07	066-04	066-04	066-04	188-97	p
B2-MM10	16:27:29.6	-24:27:42	188-97	066-04	066-04	066-04	p
B2-MM14	16:27:32.8	-24:26:29	051-00	066-04	066-04	051-00	s
B2-MM15	16:27:32.8	-24:27:03	051-00	066-04	066-04	066-04	s
B2-MM16	16:27:34.5	-24:26:12	188-97	066-04	066-04	051-00	s
B2-MM17	16:27:35.2	-24:26:21	051-00	–	–	051-00	s
C-We	16:26:50.0	-24:32:49	051-00	066-04	066-04	066-04	s
C-Ne	16:26:57.2	-24:31:39	051-00	066-04	066-04	051-00	s
C-MM3	16:26:58.9	-24:34:22	051-00	–	–	051-00	s
C-MM4	16:26:59.4	-24:34:02	051-00	–	–	051-00	s
C-MM5	16:27:00.1	-24:34:27	188-97	066-04	066-04	051-00	s
C-MM6	16:27:01.6	-24:34:37	051-00	–	–	051-00	s
C-MM7	16:27:03.3	-24:34:22	051-00	–	–	051-00	s
E-MM1e	16:26:57.7	-24:36:56	051-00	066-04	066-04	–	s
E-MM2d	16:27:04.9	-24:39:15	188-97	066-04	066-04	051-00	s
E-MM3	16:27:07.4	-24:36:01	–	–	–	188-97	s
E-MM4	16:27:10.6	-24:39:30	066-04	066-04	066-04	051-00	s
E-MM5	16:27:11.8	-24:37:57	–	–	–	188-97	s
F-MM1	16:27:22.1	-24:40:02	066-04	066-04	066-04	188-97	s
F-MM2	16:27:24.3	-24:40:35	188-97	066-04	066-04	188-97	s
H-MM1	16:27:58.3	-24:33:42	066-04	066-04	066-04	066-04	s
I-MM1	16:28:57.7	-24:20:48	066-04	066-04	066-04	066-04	s

Table A.2. Results of hfs-fitting of N_2H^+(1–0), excitation temperature T_{ex} and total column density N_{tot} calculations.

Source	$T_{ant} \cdot \tau$ (K km s^{-1})	V_{LSR} (km s^{-1})	Δv (km s^{-1})	τ	RMS T_{mb} (K)	T_{ex} (K)	N_{tot} (10^{13} cm^{-2})
A3-MM1	1.82 ± 0.12	3.205 ± 0.028	0.871 ± 0.057	0.1	0.097	7.3[a]	0.22 ± 0.02
A-MM4	17.92 ± 0.83	3.194 ± 0.003	0.449 ± 0.008	2.3 ± 0.5	0.152	11.0 ± 4.6	1.19 ± 0.28
A-MM5	15.76 ± 0.78	3.162 ± 0.004	0.508 ± 0.012	0.1	0.254	7.3	1.10 ± 0.06
VLA1623A	20.79 ± 0.52	3.635 ± 0.002	0.561 ± 0.005	4.5 ± 0.3	0.105	7.7 ± 0.9	1.60 ± 0.19
SM1N	58.19 ± 1.27	3.523 ± 0.002	0.500 ± 0.005	8.2 ± 0.3	0.244	10.2 ± 0.8	4.21 ± 0.37
SM1	44.75 ± 0.11	3.599 ± 0.001	0.589 ± 0.001	6.2 ± 0.0	0.224	10.3 ± 0.1	3.82 ± 0.30
A-MM6	5.13 ± 0.88	3.334 ± 0.017	0.724 ± 0.049	0.1	0.157	7.3	0.51 ± 0.09
SM2	23.99 ± 0.35	3.482 ± 0.001	0.467 ± 0.003	3.1 ± 0.2	0.178	10.9 ± 1.1	1.65 ± 0.15
A-MM8	21.50 ± 0.36	3.484 ± 0.001	0.371 ± 0.003	2.7 ± 0.2	0.128	11.2 ± 1.5	1.19 ± 0.12
A-S	3.28 ± 0.76	3.672 ± 0.008	0.242 ± 0.024	0.1	0.110	7.3	0.11 ± 0.03
B1-MM1	6.10 ± 1.30	4.017 ± 0.009	0.291 ± 0.024	0.1	0.186	7.3	0.24 ± 0.06
B1-MM3	28.35 ± 1.83	3.183 ± 0.012	0.248 ± 0.016	0.1	0.273	7.3	0.97 ± 0.09
	20.72 ± 2.09	3.775 ± 0.006	0.333 ± 0.014	4.3 ± 1.3	0.273	7.9 ± 4.3	0.95 ± 0.30
B1-MM4	43.15 ± 3.11	3.660 ± 0.015	0.389 ± 0.023	25.3 ± 1.9	0.369	4.6 ± 0.6	2.87 ± 0.46
	13.62 ± 2.41	3.985 ± 0.006	0.245 ± 0.014	0.1	0.369	7.3	0.46 ± 0.09
B1B2-MM1	9.56 ± 0.57	4.031 ± 0.005	0.385 ± 0.013	0.1	0.192	7.3	0.51 ± 0.03
B1B2-MM2e	3.84 ± 0.98	3.913 ± 0.026	0.570 ± 0.071	0.1	0.188	7.3	0.30 ± 0.09
B2-MM1	16.30 ± 1.55	4.009 ± 0.006	0.381 ± 0.015	4.8 ± 1.2	0.245	6.5 ± 2.8	0.87 ± 0.24
B2-MM2	9.33 ± 0.82	3.841 ± 0.023	0.628 ± 0.059	3.9 ± 0.9	0.121	5.4 ± 1.9	0.89 ± 0.25
	7.36 ± 0.94	4.303 ± 0.009	0.319 ± 0.023	0.1	0.121	7.3	0.32 ± 0.05
B2-MM6	19.64 ± 1.61	3.724 ± 0.010	0.696 ± 0.026	4.0 ± 0.8	0.303	8.0 ± 3.0	1.88 ± 0.43
B2-MM8	7.89 ± 0.84	3.463 ± 0.017	0.460 ± 0.026	10.7 ± 1.7	0.138	3.6 ± 0.6	1.01 ± 0.22
	23.63 ± 0.43	4.133 ± 0.003	0.507 ± 0.006	3.8 ± 0.2	0.138	9.3 ± 1.0	1.69 ± 0.17
B2-MM10	11.85 ± 1.04	4.293 ± 0.010	0.579 ± 0.024	0.1	0.273	7.3	0.95 ± 0.09
B2-MM14	17.13 ± 1.78	4.122 ± 0.014	0.771 ± 0.035	3.7 ± 1.0	0.236	7.7 ± 3.8	1.82 ± 0.53
B2-MM15	34.75 ± 3.16	4.372 ± 0.006	0.374 ± 0.014	6.7 ± 1.3	0.270	8.3 ± 3.0	1.80 ± 0.38
B2-MM16	17.27 ± 1.14	4.003 ± 0.008	0.640 ± 0.017	3.0 ± 0.7	0.232	8.8 ± 3.6	1.54 ± 0.37
B2-MM17	15.50 ± 1.82	4.038 ± 0.013	0.635 ± 0.032	0.1	0.236	7.3	1.36 ± 0.17
C-We	16.50 ± 1.88	3.540 ± 0.003	0.195 ± 0.009	6.7 ± 1.7	0.182	5.4 ± 2.1	0.48 ± 0.13
C-Ne	41.94 ± 1.64	3.772 ± 0.001	0.210 ± 0.003	12.3 ± 0.7	0.155	6.5 ± 0.7	1.23 ± 0.15
C-MM3	36.01 ± 0.20	3.786 ± 0.003	0.325 ± 0.003	11.8 ± 0.2	0.196	6.1 ± 0.2	1.67 ± 0.19
C-MM4	34.24 ± 6.92	3.807 ± 0.010	0.341 ± 0.021	16.3 ± 4.4	0.277	5.1 ± 2.3	1.84 ± 0.56
C-MM5	48.70 ± 1.86	3.758 ± 0.002	0.320 ± 0.004	18.3 ± 0.9	0.179	5.7 ± 0.5	2.29 ± 0.29
C-MM6	42.64 ± 1.86	3.670 ± 0.001	0.330 ± 0.004	16.9 ± 1.0	0.118	5.5 ± 0.6	2.10 ± 0.28
C-MM7	35.74 ± 2.66	3.647 ± 0.012	0.300 ± 0.015	28.1 ± 1.6	0.242	4.2 ± 0.4	2.12 ± 0.33
E-MM1e	2.51 ± 0.20	4.396 ± 0.019	0.361 ± 0.028	0.1	0.181	7.3	0.12 ± 0.01
E-MM2d	14.40 ± 0.91	4.455 ± 0.003	0.296 ± 0.008	2.8 ± 0.7	0.148	8.2 ± 3.9	0.59 ± 0.17[b]
E-MM3							
E-MM4	7.29 ± 0.42	4.197 ± 0.003	0.283 ± 0.007	2.2 ± 0.7	0.120	6.3 ± 3.0	0.29 ± 0.09
E-MM5							
F-MM1	11.02 ± 0.45	4.660 ± 0.004	0.535 ± 0.008	4.1 ± 0.5	0.143	5.7 ± 1.0	0.87 ± 0.14
F-MM2	20.95 ± 1.52	4.094 ± 0.003	0.238 ± 0.009	8.8 ± 1.2	0.147	5.4 ± 1.2	0.75 ± 0.14
	9.20 ± 0.74	4.550 ± 0.005	0.340 ± 0.013	0.1	0.147	7.3	0.43 ± 0.04
H-MM1	23.02 ± 0.47	4.223 ± 0.001	0.271 ± 0.002	3.7 ± 0.3	0.209	9.3 ± 1.2	0.88 ± 0.09
I-MM1	28.57 ± 0.74	3.296 ± 0.001	0.271 ± 0.003	8.9 ± 0.4	0.142	6.3 ± 0.5	1.09 ± 0.13

[a] In case when optical depth τ value was less than 3σ we did not calculate the excitation temperature with equation 2, but rather adopt the average of the excitation temperatures of the other cores.

[b] N_{tot} calculated assuming the line is optically thick, produce large uncertainty which propagates to the R_D uncertainty so $R_D < 2.5\ \Delta R_D$. Thus, to measure R_D for E-MM2d, $N_{tot} = (0.58 \pm 0.02) \times 10^{13}\ cm^{-2}$ calculated assuming the line is optically thin (τ = 0.1, T=7.3 K) used.

Table A.3. Results of hfs-fitting of N_2D^+(1–0)

Source	$T_{ant} \cdot \tau$ (K km s^{-1})	V_{LSR} (km s^{-1})	Δv (km s^{-1})	τ	RMS T_{mb} (K)	T_{ex} (K)	N_{tot} (10^{12} cm^{-2})
A3-MM1					0.103	7.3	<0.20
A-MM4					0.120	11.0	<0.26
A-MM5					0.120	7.3	<0.23
VLA1623a	1.56 ± 0.09	3.644 ± 0.017	0.546 ± 0.032	0.1	0.114	7.7	1.57 ± 0.13
SM1N	1.62 ± 0.06	3.639 ± 0.004	0.498 ± 0.018	0.1	0.074	10.2	1.59 ± 0.08
SM1	2.18 ± 0.08	3.660 ± 0.012	0.593 ± 0.024	0.1	0.107	10.3	2.56 ± 0.14
A-MM6					0.136	7.3	<0.26
SM2	1.06 ± 0.07	3.524 ± 0.016	0.450 ± 0.035	0.1	0.088	10.9	0.97 ± 0.10
A-MM8	0.83 ± 0.15	3.475 ± 0.015	0.171 ± 0.032	0.1	0.063	11.2	0.29 ± 0.08
A-S					0.131	7.3	<0.25
B1-MM1	1.29 ± 0.08	3.990 ± 0.012	0.392 ± 0.027	0.1	0.087	7.3	0.93 ± 0.09
B1-MM3	4.71 ± 0.43	3.855 ± 0.006	0.371 ± 0.014	6.5 ± 1.3	0.090	3.5 ± 0.5	6.22 ± 1.62
B1-MM4	3.19 ± 0.17	3.567 ± 0.008	0.259 ± 0.019	0.1	0.115	4.6	1.81 ± 0.16
	2.94 ± 0.15	3.995 ± 0.010	0.363 ± 0.029	0.1	0.115	4.6	2.34 ± 0.22
B1B2-MM1	1.76 ± 0.08	4.021 ± 0.008	0.383 ± 0.018	0.1	0.086	7.3	1.24 ± 0.08
B1B2-MM2					0.135	7.3	<0.26
B2-MM1	1.77 ± 0.09	4.082 ± 0.008	0.374 ± 0.021	0.1	0.092	6.5	1.22 ± 0.09
B2-MM2	1.00 ± 0.07	4.194 ± 0.029	0.752 ± 0.053	0.1	0.100	5.4	1.46 ± 0.15
B2-MM6	2.38 ± 0.07	3.840 ± 0.013	0.759 ± 0.024	0.1	0.107	8.0	3.34 ± 0.15
B2-MM8	0.78 ± 0.06	3.901 ± 0.048	1.241 ± 0.114	0.1	0.104	9.3	1.85 ± 0.23
B2-MM10					0.119	7.3	<0.23
B2-MM14	1.46 ± 0.10	4.129 ± 0.035	0.622 ± 0.049	0.1	0.129	7.0	1.67 ± 0.17
B2-MM15	0.95 ± 0.10	4.365 ± 0.018	0.350 ± 0.045	0.1	0.101	7.3	0.61 ± 0.10
B2-MM16	1.85 ± 0.08	3.877 ± 0.016	0.606 ± 0.019	0.1	0.127	8.8	2.11 ± 0.11
B2-MM17							
C-We	1.63 ± 0.10	3.575 ± 0.007	0.236 ± 0.015	0.1	0.088	5.4	0.75 ± 0.07
C-N	10.07 ± 0.65	3.795 ± 0.002	0.228 ± 0.006	6.4 ± 0.9	0.127	4.4 ± 0.7	5.25 ± 1.08
C-MM3							
C-MM4							
C-MM5	7.42 ± 0.49	3.881 ± 0.003	0.282 ± 0.008	2.5 ± 0.8	0.127	5.9 ± 2.4	3.93 ± 1.29
C-MM6							
C-MM7							
E-MM1					0.113	7.3	<0.22
E-MM2d	5.91 ± 0.53	4.485 ± 0.004	0.295 ± 0.011	4.9 ± 1.2	0.115	4.0 ± 1.0	4.51 ± 1.30[a]
E-MM3							
E-MM4	0.82 ± 0.07	4.288 ± 0.016	0.357 ± 0.033	0.1	0.081	6.3	0.55 ± 0.07
E-MM5							
F-MM1					0.087	5.7	<0.18
F-MM2	1.03 ± 0.09	4.276 ± 0.033	0.767 ± 0.069	0.1	0.121	5.4	1.54 ± 0.19
H-MM1	6.95 ± 0.30	4.243 ± 0.002	0.280 ± 0.005	2.7 ± 0.5	0.081	5.5 ± 1.4	3.76 ± 0.86
I-MM1	5.88 ± 0.31	3.325 ± 0.002	0.283 ± 0.006	2.8 ± 0.6	0.079	5.0 ± 1.4	3.40 ± 0.89

[a] N_{tot} calculated assuming the line is optically thick, produce large uncertainty which propagates to the R_D uncertainty so $R_D < 2.5\ \Delta R_D$. Thus, to measure R_D for E-MM2d, $N_{tot} = (2.41 \pm 0.07) \times 10^{12}\ cm^{-2}$ calculated assuming the line is optically thin ($\tau = 0.1$, T=7.3 K) used.

Table A.4. Results of hfs-fitting of N_2D^+(2–1)

Source	$T_{ant} \cdot \tau$ (K km s^{-1})	V_{LSR} (km s^{-1})	Δv (km s^{-1})	τ	RMS T_{mb} (K)	T_{ex} (K)	N_{tot} (10^{12} cm^{-2})
A3-MM1					0.186	7.3	<0.22
A-MM4	1.10 ± 0.15	3.169 ± 0.019	0.303 ± 0.047	0.1	0.170	11.0	0.31 ± 0.06
A-MM5					0.275	7.3	<0.32
VLA1623A	4.13 ± 0.08	3.653 ± 0.006	0.549 ± 0.009	0.1	0.268	7.7	2.43 ± 0.06
SM1N	5.42 ± 0.25	3.627 ± 0.004	0.468 ± 0.011	1.2 ± 0.2	0.139	8.0 ± 3.3	2.64 ± 0.45
SM1	3.38 ± 0.37	3.754 ± 0.011	0.493 ± 0.028	1.6 ± 0.5	0.202	5.6 ± 3.9	2.54 ± 0.83
A-MM6					0.183	7.3	<0.22
SM2	2.74 ± 0.15	3.435 ± 0.008	0.311 ± 0.019	0.1	0.193	10.9	0.79 ± 0.06
A-MM8	1.42 ± 0.23	3.411 ± 0.035	0.383 ± 0.068	0.1	0.223	11.2	0.50 ± 0.12
A-S					0.178	7.3	<0.21
B1-MM1	1.84 ± 0.32	3.952 ± 0.023	0.298 ± 0.060	0.1	0.215	7.3	0.61 ± 0.16
B1-MM3	3.53 ± 0.29	3.747 ± 0.011	0.321 ± 0.032	0.1	0.365	7.9	1.19 ± 0.15
B1-MM4	1.85 ± 0.17	3.752 ± 0.036	0.702 ± 0.066	0.1	0.309	4.6	2.84 ± 0.37
B1B2-MM1	2.11 ± 0.27	3.978 ± 0.016	0.274 ± 0.041	0.1	0.310	7.3	0.65 ± 0.13
B1B2-MM2e							
B2-MM1	3.23 ± 0.21	3.967 ± 0.010	0.286 ± 0.019	0.1	0.294	6.5	1.15 ± 0.11
B2-MM2	1.73 ± 0.14	4.072 ± 0.030	0.743 ± 0.070	0.1	0.192	5.4	2.06 ± 0.26
B2-MM6	3.90 ± 0.14	3.785 ± 0.013	0.735 ± 0.031	0.1	0.335	8.0	2.99 ± 0.17
B2-MM8	1.83 ± 0.14	4.160 ± 0.017	0.435 ± 0.036	0.1	0.253	9.3	0.77 ± 0.09
B2-MM10					0.326	7.3	<0.38
B2-MM14	3.97 ± 0.11	4.160 ± 0.006	0.426 ± 0.014	0.1	0.197	7.0	1.96 ± 0.08
B2-MM15	1.00 ± 0.14	4.305 ± 0.029	0.446 ± 0.076	0.1	0.107	7.3	0.50 ± 0.11
B2-MM16	4.59 ± 0.13	3.921 ± 0.008	0.611 ± 0.021	0.1	0.266	8.8	2.77 ± 0.13
B2-MM17							
C-W	1.40 ± 0.27	3.507 ± 0.018	0.239 ± 0.057	0.1	0.160	5.4	0.54 ± 0.17
C-N	12.80 ± 0.93	3.743 ± 0.004	0.175 ± 0.009	6.4 ± 0.7	0.235	5.4 ± 1.4	3.59 ± 0.46
C-MM3							
C-MM4							
C-MM5	7.83 ± 0.98	3.829 ± 0.006	0.222 ± 0.018	4.2 ± 0.9	0.270	5.2 ± 2.5	2.96 ± 0.67
C-MM6							
C-MM7							
E-MM1					0.222	7.3	<0.26
E-MM2D	12.07 ± 0.80	4.413 ± 0.004	0.232 ± 0.010	3.2 ± 0.4	0.247	7.3 ± 2.5	3.11 ± 0.43
E-MM3							
E-MM4	1.06 ± 0.20	4.187 ± 0.026	0.295 ± 0.061	0.1	0.168	6.3	0.41 ± 0.11
E-MM5							
F-MM1					0.230	5.7	<0.36
F-MM2	1.21 ± 0.10	4.244 ± 0.032	0.948 ± 0.100	0.1	0.197	5.4	1.83 ± 0.25
H-MM1	19.87 ± 0.74	4.208 ± 0.002	0.217 ± 0.005	4.4 ± 0.3	0.209	8.1 ± 1.4	4.44 ± 0.31
I-MM1	5.49 ± 0.55	3.242 ± 0.005	0.259 ± 0.015	2.0 ± 0.5	0.194	6.3 ± 3.9	1.84 ± 0.51

Table A.5. Results of hfs-fitting of $C^{17}O(1–0)$ and column density calculations

Source	$T_{ant} \cdot \tau$ (K km s^{-1})	V_{LSR} (km s^{-1})	Δv (km s^{-1})	τ	RMS T_{mb} (K)	T_{ex} (K)	N_{tot} (10^{15} cm^{-2})
A3-MM1	0.61 ± 0.08	3.050 ± 0.123	1.678 ± 0.223	0.1	0.154	17.6	1.32 ± 0.24
A-MM4	1.88 ± 0.12	3.152 ± 0.027	0.829 ± 0.066	0.1	0.198	16.3	1.92 ± 0.20
A-MM5	2.65 ± 0.21	3.186 ± 0.019	0.673 ± 0.069	0.1	0.210	18.6	2.37 ± 0.30
VLA1623a	3.35 ± 0.09	3.714 ± 0.007	0.755 ± 0.025	0.1	0.114	16.4	3.13 ± 0.13
SM1N	5.98 ± 0.16	3.524 ± 0.006	0.540 ± 0.015	0.1	0.152	17.3	4.11 ± 0.16
	0.90 ± 0.10	3.096 ± 0.097	1.812 ± 0.111	0.1	0.152	17.3	2.09 ± 0.27
SM1	7.77 ± 0.09	3.659 ± 0.004	0.696 ± 0.010	0.1	0.134	17.2	6.86 ± 0.13
A-MM6	3.30 ± 0.11	3.094 ± 0.013	0.961 ± 0.040	0.1	0.209	18.8	4.24 ± 0.23
SM2	4.06 ± 0.12	3.492 ± 0.010	0.796 ± 0.029	0.1	0.159	18.5	4.28 ± 0.20
B1-MM1	1.60 ± 0.06	3.625 ± 0.020	1.158 ± 0.045	0.1	0.192	16.3	2.29 ± 0.12
B1-MM3	2.12 ± 0.07	3.480 ± 0.015	0.984 ± 0.038	0.1	0.202	16.4	2.58 ± 0.13
B1-MM4	2.61 ± 0.13	3.542 ± 0.024	1.030 ± 0.067	0.1	0.223	13.0	2.97 ± 0.25
B1B2-MM1	1.33 ± 0.05	3.696 ± 0.026	1.403 ± 0.060	0.1	0.204	13.3	2.09 ± 0.12
B1B2-MM2	1.65 ± 0.05	4.127 ± 0.020	1.537 ± 0.049	0.1	0.206	15.8	3.08 ± 0.13
B2-MM1	1.70 ± 0.11	3.772 ± 0.021	0.752 ± 0.060	0.1	0.268	14.1	1.46 ± 0.15
B2-MM2	0.97 ± 0.07	3.915 ± 0.033	1.054 ± 0.085	0.1	0.231	14.2	1.18 ± 0.13
B2-MM6	0.81 ± 0.06	3.362 ± 0.054	1.444 ± 0.112	0.1	0.246	13.2	1.30 ± 0.14
B2-MM8	0.79 ± 0.09	3.402 ± 0.137	2.124 ± 0.259	0.1	0.171	14.5	1.94 ± 0.33
B2-MM10	0.86 ± 0.05	3.427 ± 0.059	1.944 ± 0.104	0.1	0.231	14.0	1.90 ± 0.15
B2-MM14	0.84 ± 0.09	3.602 ± 0.093	1.563 ± 0.173	0.1	0.172	14.6	1.52 ± 0.24
B2-MM15	1.10 ± 0.10	3.370 ± 0.040	1.135 ± 0.143	0.1	0.235	13.9	1.42 ± 0.22
B2-MM16	1.24 ± 0.05	3.632 ± 0.021	1.067 ± 0.049	0.1	0.102	14.3	1.53 ± 0.09
B2-MM17	1.32 ± 0.12	3.636 ± 0.062	1.353 ± 0.125	0.1	0.180	14.3	2.06 ± 0.26
C-We	3.39 ± 0.06	3.715 ± 0.008	0.688 ± 0.016	0.1	0.217	12.0	2.50 ± 0.07
	2.07 ± 0.09	4.395 ± 0.010	0.398 ± 0.016	0.1	0.217	12.0	0.88 ± 0.05
C-Ne	3.82 ± 0.11	3.744 ± 0.009	0.782 ± 0.029	0.1	0.153	12.0	3.21 ± 0.15
C-MM3	6.37 ± 0.21	3.716 ± 0.009	0.626 ± 0.026	0.1	0.228	12.3	4.32 ± 0.23
C-MM4	6.10 ± 0.21	3.721 ± 0.009	0.598 ± 0.026	0.1	0.212	10.4	3.75 ± 0.21
	1.72 ± 0.21	4.911 ± 0.026	0.413 ± 0.056	0.1	0.212	10.4	0.73 ± 0.13
C-MM5	5.15 ± 0.26	3.692 ± 0.008	0.423 ± 0.026	0.1	0.227	10.7	2.26 ± 0.18
	1.05 ± 0.18	3.962 ± 0.114	2.140 ± 0.225	0.1	0.227	10.7	2.33 ± 0.46
C-MM6	5.07 ± 0.15	3.676 ± 0.008	0.709 ± 0.028	0.1	0.173	13.0	3.98 ± 0.20
	1.93 ± 0.18	4.855 ± 0.012	0.266 ± 0.031	0.1	0.173	13.0	0.57 ± 0.09
C-MM7	5.94 ± 0.28	3.691 ± 0.012	0.591 ± 0.033	0.1	0.307	12.0	3.77 ± 0.27
E-MM2d	1.27 ± 0.03	3.447 ± 0.016	1.128 ± 0.029	0.1	0.080	13.6	1.62 ± 0.05
	1.90 ± 0.07	3.930 ± 0.005	0.243 ± 0.009	0.1	0.080	13.6	0.52 ± 0.03
	1.29 ± 0.04	4.502 ± 0.014	0.623 ± 0.022	0.1	0.080	13.6	0.91 ± 0.04
E-MM3	1.02 ± 0.15	3.700 ± 0.099	2.261 ± 0.184	0.1	0.175	15.0	2.71 ± 0.46
	2.09 ± 0.20	3.477 ± 0.022	0.600 ± 0.066	0.1	0.175	15.0	1.48 ± 0.21
E-MM4	2.04 ± 0.04	3.427 ± 0.022	1.369 ± 0.042	0.1	0.108	15.0	3.30 ± 0.12
	1.16 ± 0.14	4.197 ± 0.011	0.216 ± 0.035	0.1	0.108	15.0	0.30 ± 0.06
E-MM5	2.42 ± 0.11	3.314 ± 0.023	0.952 ± 0.065	0.1	0.176	15.0	2.72 ± 0.22
	1.63 ± 0.16	4.549 ± 0.031	0.603 ± 0.083	0.1	0.176	15.0	1.16 ± 0.20
F-MM1	2.54 ± 0.09	3.690 ± 0.024	1.411 ± 0.057	0.1	0.217	15.3	4.27 ± 0.23
F-MM2	2.49 ± 0.10	3.725 ± 0.023	1.230 ± 0.055	0.1	0.206	15.6	3.68 ± 0.22
H-MM1	1.38 ± 0.12	3.957 ± 0.029	0.726 ± 0.083	0.1	0.213	11.0	1.04 ± 0.15
I-MM1	1.74 ± 0.13	3.231 ± 0.010	0.277 ± 0.025	0.1	0.206	10.0	0.49 ± 0.06

Table A.6. Results of hfs-fitting of $C^{17}O$(2–1) and column density calculations

Source	$T_{ant} \cdot \tau$ (K km s^{-1})	V_{LSR} (km s^{-1})	Δv (km s^{-1})	τ	RMS (K)	T_{ex} (K)	N_{tot} (10^{15} cm^{-2})
A3-MM1	3.94 ± 0.55	2.513 ± 0.051	0.702 ± 0.110	0.1	0.846	17.6	1.57 ± 0.33
A-MM4	6.85 ± 0.62	3.231 ± 0.034	0.682 ± 0.067	0.1	0.966	16.3	2.66 ± 0.36
	1.64 ± 0.79	5.071 ± 0.115	0.523 ± 0.289	0.1	0.966	16.3	0.49 ± 0.36
A-MM5	9.12 ± 0.70	3.208 ± 0.025	0.634 ± 0.052	0.1	1.068	18.6	3.29 ± 0.37
VLA1623a	9.53 ± 0.40	3.733 ± 0.017	0.820 ± 0.039	0.1	0.401	16.4	4.46 ± 0.28
SM1N	15.79 ± 0.47	3.496 ± 0.006	0.469 ± 0.018	0.1	0.308	17.3	4.21 ± 0.21
	4.53 ± 0.28	3.011 ± 0.050	1.834 ± 0.078	0.1	0.308	17.3	4.72 ± 0.35
SM1	35.26 ± 1.71	3.667 ± 0.006	0.638 ± 0.015	1.8 ± 0.2	0.572	17.2	7.95 ± 0.92
A-MM6	12.29 ± 0.54	3.038 ± 0.021	0.942 ± 0.046	0.1	0.966	18.8	6.60 ± 0.43
SM2	10.29 ± 0.67	3.322 ± 0.030	0.937 ± 0.045	0.1	0.699	18.5	5.49 ± 0.44
	8.54 ± 0.99	3.615 ± 0.015	0.274 ± 0.042	0.1	0.699	18.5	1.33 ± 0.26
A-MM8	7.62 ± 1.18	3.446 ± 0.034	0.414 ± 0.065	0.1	0.950	18.4	1.80 ± 0.40
B1-MM1	4.04 ± 0.43	3.611 ± 0.061	1.235 ± 0.155	0.1	0.516	16.3	2.84 ± 0.47
B1-MM4	5.65 ± 0.68	3.587 ± 0.063	0.969 ± 0.124	0.1	1.298	13.0	3.27 ± 0.57
B1B2-MM1	3.03 ± 0.30	3.633 ± 0.076	1.697 ± 0.199	0.1	0.476	13.3	3.04 ± 0.47
B1B2-MM2	3.34 ± 0.26	4.148 ± 0.063	1.931 ± 0.190	0.1	0.419	15.8	3.69 ± 0.46
B2-MM1	3.62 ± 0.39	3.826 ± 0.053	1.041 ± 0.125	0.1	0.430	14.1	2.20 ± 0.35
B2-MM2	1.88 ± 0.14	3.782 ± 0.047	1.072 ± 0.086	0.1	0.301	14.2	1.18 ± 0.13
B2-MM8	1.70 ± 0.21	3.380 ± 0.121	1.875 ± 0.248	0.1	0.416	14.5	1.84 ± 0.33
B2-MM14	1.90 ± 0.30	3.676 ± 0.137	1.632 ± 0.278	0.1	0.519	14.6	1.80 ± 0.42
B2-MM16	2.73 ± 0.14	3.662 ± 0.032	1.162 ± 0.065	0.1	0.181	14.3	1.85 ± 0.14
C-W	3.70 ± 0.33	3.698 ± 0.329	1.626 ± 0.167	0.1	0.531	12.0	3.71 ± 0.50
C-MM3	1.97 ± 0.24	3.906 ± 0.070	2.602 ± 0.231	0.1	0.259	12.3	3.12 ± 0.47
	5.31 ± 0.36	3.657 ± 0.014	0.500 ± 0.042	0.1	0.259	12.3	1.62 ± 0.18
C-MM4	8.91 ± 0.77	3.716 ± 0.030	0.765 ± 0.081	0.1	0.662	10.4	4.57 ± 0.62
C-MM5	5.31 ± 0.36	3.657 ± 0.014	0.499 ± 0.042	0.1	0.241	10.7	1.74 ± 0.19
	1.97 ± 0.24	3.905 ± 0.070	2.599 ± 0.231	0.1	0.241	10.7	3.37 ± 0.50
C-MM6	3.99 ± 0.62	3.605 ± 0.035	0.557 ± 0.090	0.1	0.411	13.0	1.33 ± 0.30
	2.52 ± 0.40	3.702 ± 0.090	2.423 ± 0.242	0.1	0.411	13.0	3.64 ± 0.68
C-MM7	2.97 ± 0.36	3.772 ± 0.105	1.593 ± 0.208	0.1	0.607	12.0	2.92 ± 0.52
E-MM1	4.51 ± 0.61	3.764 ± 0.053	0.706 ± 0.165	0.1	0.505	15.0	1.83 ± 0.50
	2.57 ± 0.54	4.694 ± 0.106	0.681 ± 0.199	0.1	0.505	15.0	1.01 ± 0.36
E-MM2d	3.10 ± 0.27	3.823 ± 0.047	1.324 ± 0.136	0.1	0.322	13.6	2.41 ± 0.32
E-MM3	2.94 ± 0.27	3.449 ± 0.099	2.580 ± 0.308	0.1	0.907	15.0	4.37 ± 0.66
E-MM4	3.26 ± 0.20	3.604 ± 0.049	1.708 ± 0.128	0.1	0.301	15.0	3.21 ± 0.31
E-MM5	3.90 ± 0.30	3.882 ± 0.068	2.030 ± 0.191	0.1	0.859	15.0	4.56 ± 0.55
F-MM1	4.53 ± 0.19	3.717 ± 0.028	1.324 ± 0.070	0.1	0.252	15.3	3.44 ± 0.23
	3.20 ± 0.44	4.732 ± 0.017	0.222 ± 0.021	0.1	0.252	15.3	0.41 ± 0.07
F-MM2	4.10 ± 0.18	3.774 ± 0.030	1.517 ± 0.079	0.1	0.233	15.6	3.56 ± 0.24

Table A.7. Column density, deuterium fraction and CO-depletion factor

Source	$N_{tot}(N_2H^+)$ (10^{13} cm^{-2})	$N_{tot}(N_2D^+)$ (10^{12} cm^{-2})	R_D	$S_{850\mu m}$ (Jy beam^{-1})	T_k^a (K)	T_k ref.^{b}	$N(H_2)$ (10^{22} cm^{-2})	$N_{tot}(C^{17}O)$ (10^{15} cm^{-2})	f_d
A3-MM1	0.22 ± 0.02	<0.20	<0.09	262 ± 35	17.6 ± 0.7	P	1.00 ± 0.13	1.32 ± 0.24	0.66 ± 0.15
A-MM4	1.19 ± 0.28	<0.26	<0.02	541 ± 46	16.3 ± 0.5	P	2.34 ± 0.20	1.92 ± 0.20	1.06 ± 0.14
A-MM5	1.10 ± 0.06	<0.23	<0.02	1035 ± 59	18.6 ± 0.7	P	3.64 ± 0.21	2.37 ± 0.30	1.33 ± 0.18
VLA1623	1.60 ± 0.19	1.57 ± 0.13	0.10 ± 0.01	4887 ± 108	16.4 ± 0.5	P	20.89 ± 0.46	3.13 ± 0.13	5.80 ± 0.27
SM1N	4.21 ± 0.37	1.59 ± 0.08	0.038 ± 0.004	5760 ± 77	17.3 ± 0.6	P	22.63 ± 0.30	6.20 ± 0.31	3.17 ± 0.16
SM1	3.82 ± 0.30	2.56 ± 0.14	0.067 ± 0.006	8601 ± 84	17.2 ± 0.6	P	34.10 ± 0.33	6.86 ± 0.13	4.32 ± 0.09
A-MM6	0.51 ± 0.09	<0.26	<0.05	1864 ± 67	18.8 ± 0.8	P	6.44 ± 0.23	4.24 ± 0.23	1.32 ± 0.09
SM2	1.65 ± 0.15	0.97 ± 0.10	0.059 ± 0.008	3746 ± 45	18.5 ± 0.7	P	13.27 ± 0.16	4.28 ± 0.20	2.69 ± 0.13
A-MM8	1.19 ± 0.12	0.29 ± 0.08	0.024 ± 0.007	1065 ± 42	18.4 ± 0.7	P	3.80 ± 0.15		
A-S	0.11 ± 0.03	<0.25	<0.23	109 ± 40	20	M	0.34 ± 0.13		
B1-MM1	0.24 ± 0.06	0.93 ± 0.09	0.39 ± 0.10	131 ± 39	16.3 ± 1.9	F	0.57 ± 0.17	2.29 ± 0.12	0.22 ± 0.07
B1-MM3	1.92 ± 0.31	6.22 ± 1.62	0.32 ± 0.10	706 ± 20	12.2 ± 0.3	P	5.02 ± 0.14	2.25 ± 0.11	1.94 ± 0.11
B1-MM4	3.33 ± 0.47	4.15 ± 0.27	0.12 ± 0.02	528 ± 31	11.8 ± 0.2	P	3.99 ± 0.23	2.87 ± 0.24	1.21 ± 0.12
B1B2-MM1	0.51 ± 0.03	1.24 ± 0.08	0.24 ± 0.02	216 ± 47	13.3 ± 1.2	F	1.31 ± 0.28	2.09 ± 0.12	0.55 ± 0.12
B1B2-MM2	0.30 ± 0.09	<0.26	<0.09	107 ± 27	15.8 ± 0.5	P	0.49 ± 0.12	3.08 ± 0.13	0.14 ± 0.03
B2-MM1	0.87 ± 0.24	1.22 ± 0.09	0.14 ± 0.04	207 ± 39	14.1	F	1.14 ± 0.21	1.46 ± 0.15	0.68 ± 0.15
B2-MM2	1.21 ± 0.25	1.46 ± 0.15	0.12 ± 0.03	470 ± 40	11.4 ± 0.2	P	3.80 ± 0.32	1.08 ± 0.12	3.06 ± 0.43
B2-MM6	1.88 ± 0.43	3.34 ± 0.15	0.18 ± 0.04	1190 ± 35	11.3 ± 0.2	P	9.78 ± 0.28	1.23 ± 0.13	6.91 ± 0.76
B2-MM8	2.70 ± 0.28	1.85 ± 0.23	0.07 ± 0.01	1447 ± 34	13.5 ± 0.4	P	8.57 ± 0.20	1.87 ± 0.32	3.98 ± 0.69
B2-MM10	0.95 ± 0.09	<0.23	<0.02	1026 ± 41	15.8 ± 0.5	P	4.66 ± 0.19	2.02 ± 0.15	2.00 ± 0.17
B2-MM14	1.82 ± 0.53	1.67 ± 0.17	0.09 ± 0.03	1135 ± 29	10.7 ± 0.2	P	10.38 ± 0.27	1.35 ± 0.21	6.68 ± 1.05
B2-MM15	1.80 ± 0.38	0.61 ± 0.10	0.03 ± 0.01	834 ± 32	11.8 ± 0.3	P	6.31 ± 0.24	1.33 ± 0.20	4.12 ± 0.64
B2-MM16	1.54 ± 0.37	2.11 ± 0.11	0.14 ± 0.03	1001 ± 30	10.4 ± 0.2	P	9.69 ± 0.29	1.36 ± 0.08	6.19 ± 0.41
B2-MM17	1.36 ± 0.17	—	—	864 ± 30	13.4 ± 0.3	P	5.19 ± 0.18	2.00 ± 0.26	2.25 ± 0.30
C-We	0.48 ± 0.13	0.75 ± 0.07	0.16 ± 0.04	179 ± 34	12	M	1.31 ± 0.25	3.38 ± 0.09	0.34 ± 0.07
C-Ne	1.23 ± 0.15	5.25 ± 1.08	0.43 ± 0.10	412 ± 27	12	M	3.02 ± 0.20	3.21 ± 0.15	0.82 ± 0.07
C-MM3	1.67 ± 0.19	—	—	1224 ± 29	12.3 ± 0.3	P	8.57 ± 0.20	4.32 ± 0.23	1.72 ± 0.10
C-MM4	1.84 ± 0.56	—	—	1066 ± 32	10.4 ± 0.7	F	10.32 ± 0.31	4.48 ± 0.25	2.00 ± 0.13
C-MM5	2.29 ± 0.29	3.93 ± 1.29	0.17 ± 0.06	1176 ± 29	10.7 ± 0.8	F	10.75 ± 0.27	4.59 ± 0.49	2.04 ± 0.22
C-MM6	2.10 ± 0.28	—	—	976 ± 31	12.8 ± 0.4	P	6.18 ± 0.20	4.55 ± 0.22	1.18 ± 0.07
C-MM7	2.12 ± 0.33	—	—	450 ± 42	12	M	3.30 ± 0.30	3.77 ± 0.27	0.76 ± 0.09
E-MM1e	0.12 ± 0.01	<0.22	<0.18	34 ± 36	15	M	0.17 ± 0.18		
E-MM2d	0.59 ± 0.17	4.51 ± 1.30	0.42 ± 0.02	655 ± 36	13.6 ± 0.4	P	3.83 ± 0.21	3.05 ± 0.07	1.09 ± 0.07
E-MM3	—	—	—	217 ± 31	15	M	1.07 ± 0.15	4.19 ± 0.50	0.22 ± 0.04
E-MM4	0.29 ± 0.09	0.55 ± 0.07	0.19 ± 0.06	369 ± 53	15	M	1.83 ± 0.26	3.60 ± 0.13	0.44 ± 0.07
E-MM5	—	—	—	363 ± 41	15	M	1.79 ± 0.20	3.88 ± 0.30	0.40 ± 0.05
F-MM1	0.87 ± 0.14	<0.18	<0.02	741 ± 41	15.3 ± 0.5	P	3.55 ± 0.20	4.27 ± 0.23	0.72 ± 0.06
F-MM2	1.18 ± 0.15	1.54 ± 0.19	0.13 ± 0.02	760 ± 41	15.6 ± 0.5	P	3.52 ± 0.19	3.68 ± 0.22	0.83 ± 0.07
H-MM1	0.88 ± 0.09	3.76 ± 0.86	0.43 ± 0.11	614 ± 99	11 ± 0.2	P	5.32 ± 0.86	1.04 ± 0.15	4.44 ± 0.96
I-MM1	1.09 ± 0.13	3.40 ± 0.89	0.31 ± 0.09	392 ± 135	11		4.11 ± 1.41	0.49 ± 0.06	7.30 ± 2.66

[a]We assume gas and dust to have the same temperature. [b]Temperature taken from: P — Pattle et al. (2015), F — Friesen et al. (2009), M — Motte et al. (1998).